ELLIPTICAL CAVITY DESIGNS, FABRICATIONS AND EXPERIMENTS TO INVESTIGATE CELL MISALIGNMENT AND SURFACE ROUGHNESS EFFECTS

A Thesis Submitted to
the Graduate School of Engineering and Sciences of
İzmir Institute of Technology
in Partial Fulfillment of the Requirements for the Degree of

MASTER OF SCIENCE

in Electronics and Communication Engineering

by
Anıl KARATAY

December 2019
İZMİR

We approve the thesis of **Anıl KARATAY**

Examining Committee Members:

_____
Asst. Prof. Dr. Fatih YAMAN
Department of Electrical and Electronics Engineering
İzmir Institute of Technology

_____
Prof. Dr. Mehmet Salih DİNLEYİCİ
Department of Electrical and Electronics Engineering
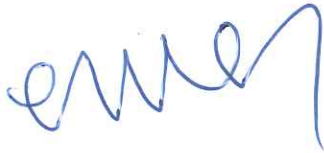İzmir Institute of Technology

_____
Prof. Dr. Abbas Kenan ÇİFTÇİ
Department of Physics
İzmir University of Economics

18 December 2019

_____
Asst. Prof. Dr. Fatih YAMAN
Supervisor, Department of Electrical and Electronics Engineering
İzmir Institute of Technology

_____
Prof. Dr. Enver TATLICIOĞLU
Head of the Department of
Electrical and Electronics Engineering

_____
Prof. Dr. Mehtap EMİRDAĞ EANES
Dean of the Graduate School of
Engineering and Sciences

ACKNOWLEDGMENTS

ABSTRACT

ELLIPTICAL CAVITY DESIGNS, FABRICATIONS AND EXPERIMENTS TO INVESTIGATE CELL MISALIGNMENT AND SURFACE ROUGHNESS EFFECTS

In this thesis, the results of 5 different elliptical cavity designs at different cell numbers and frequencies and the fabrication and measurement of two of these are presented in order to investigate the effects of cell alignment error and surface roughness. First, a 9-cell, 3.9 GHz elliptical cavity with very poor cell-to-cell coupling is designed and the acceleration parameters are optimized. Thanks to the low cell-to-cell coupling, it is aimed to better observe possible mechanical defects and the effects of cell alignment errors in this cavity on the fundamental cavity parameters and particle-cavity interaction are investigated using CST-MWS program. In addition, the effect of surface roughness of the cavity on wake fields and impedances is among the parameters that are tried to be observed. Second, a 3-cell 2 GHz cavity and its scaled version, 3-cell 3.9 GHz cavity, are designed to demonstrate that the effects of cell misalignment were not limited to only this geometry, and similar simulations are repeated for these cavities. In the experimental part of the thesis, a 3-cell 3.9 GHz elliptical cavity with high cell-to-cell coupling is designed and fabricated with a 3D printer and made conductive by nickel and copper coating techniques. Then, the effects of cell misalignment on the quality factor and the electric field on the acceleration axis are investigated experimentally. For these processes, bead-pull measurement is utilized in addition to weak and critical coupling measurements. In the last part, a 2.45 GHz single cell aluminum cavity is fabricated, the same experiments are repeated and it is experimentally demonstrated that similar effects can also be observed with higher conductivity values.

ÖZET

HÜCRE HİZASIZLIĞI VE YÜZEY PÜRÜZLÜLÜĞÜ ETKİLERİNİ ARAŞTIRMAK İÇİN ELİPTİK KAVİTE TASARIMLARI, ÜRETİMLERİ VE DENEYLERİ

Bu tezde, hücre hizalama hatası ve yüzey pürüzlülüğü etkilerinin araştırılması amacıyla, farklı hücre sayıları ve frekanslarda 5 farklı eliptik kavitenin tasarımı ve bu kavitelerden ikisinin üretilip ölçülmesine ait sonuçlar sunulmuştur. İlk olarak, hücreden hücreye kuplajı oldukça zayıf olan, 9 hücreli, 3.9 GHz bir eliptik kavite tasarlanmış ve hızlandırma parametreleri optimize edilmiştir. Hücreden hücreye kuplajın düşük olması sayesinde olası mekanik kusurların daha iyi gözlemlenmesi hedeflenmiş ve CST-MWS programı kullanılarak bu kavitedeki hücre hizalama hatalarının temel kavite parametreleri ve parçacık-kavite etkileşimi üzerindeki etkileri incelenmiştir. Buna ek olarak, kavite yüzey pürüzünün, uyarma alanlarına ve empedanslarına olan etkisi de gözlemlenmeye çalışılan parametreler arasındadır. Ardından, hücre hizalama hatasının etkilerinin yalnızca bu geometriyle sınırlı olmadığını gösterme amacıyla 3 hücreli 2 GHz'lik bir kavite ve onun ölçeklendirilmiş versiyonu olan 3 hücreli 3.9 GHz'lik bir kavite tasarlanmış ve benzer simülasyonlar bu kaviteler için de tekrarlanmıştır. Tezin deneysel kısmında, 3 hücreli 3.9 GHz eliptik bir kavite tasarlanıp 3 boyutlu yazıcıyla üretilmiş, nikel ve bakır kaplama yöntemleriyle iletken hale getirilmiştir. Ardından, hücre hizalama hatasının kalite faktörü ve hızlandırma eksenindeki elektrik alan üzerindeki etkileri deneysel olarak incelenmiştir. Bu işlemler için zayıf ve kritik kuplaj ölçümlerinin yanı sıra boncuk çekme ölçümünden de faydalanılmıştır. Tezin son kısmında ise 2.45 GHz'lik tek hücreli, alüminyum bir kavite üretilip aynı deneyler tekrarlanmış ve benzer etkilerin daha yüksek iletkenlik değerleriyle de görülebileceği deneysel olarak gösterilmiştir.

TABLE OF CONTENTS

LIST OF FIGURES

LIST OF TABLES

LIST OF ABBREVIATIONS

DC . . . . Direct Current

RF . . . . Radio Frequency

TM . . . . Transverse Magnetic

TE . . . . Transverse Electric

TEM . . . . Transverse Electromagnetic

CERN . . . . Conseil Européen pour la Recherche Nucléaire

RFQ . . . . Radio Frequency Quadrupole

Linac . . . . Linear Accelerator

JLAB . . . . Jefferson Laboratory

CST-MWS . . . . Computer Simulation Technology Microwave Studio

HFSS . . . . High Frequency Structure Simulator

FDTD . . . . Finite Difference Time Domain

MAFIA . . . . Maxwell Finite Integration Algorithm

ADS . . . . Advance Design System

E-Solver . . . . Eigenmode Solver

S-matrix . . . . Scattering Matrix

CPU . . . . Central Processing Unit

PSEF . . . . Peak surface electric field

PSMFD . . . . Peak surface magnetic flux density

CF . . . . Coupling Factor

TTF . . . . Transit Time Factor

CTCC . . . . Cell-to-Cell Coupling

FEM . . . . Finite Element Method

F-Solver . . . . Frequency Domain Solver

CNC . . . . Computer Numerical Control

PLA . . . . Polylactic Acid

ABS . . . . Acrylonitrile-Butadlene-Styrene

VNA . . . . Vector Network Analyzer

ISM . . . . Industrial Scientific and Medical

CHAPTER 1

INTRODUCTION

Accelerating technologies, which pioneer modern science today, began their fast-paced journey in 1878 with Crookes Tube (Crookes, 1878). The structure proposed by William Crookes created an electric field using DC voltage between anode and cathode inside a vacuum tube, and accelerated charged ions. However, if the DC voltage is considered as pulling and releasing a swing once, the RF voltage can be considered to surf in a wavy sea. In the first case, the potential energy gained can be used only once and the person riding the swing may fall to the ground in case of the height is too high just like DC breakdown. On the other hand, it is possible to benefit from the energy of each wave coming in a wavy sea similar to RF accelerators if you are on the correct phase. The first RF accelerator by applying alternating current between drift tubes was proposed in 1924 (Ising, 1924; Porsuk, 2015), and starting from this work, the first RF accelerator was experimentally implemented in 1928 (Wideroe, 1928; Ozcan, 2018), as illustrated in Figure 1.1.
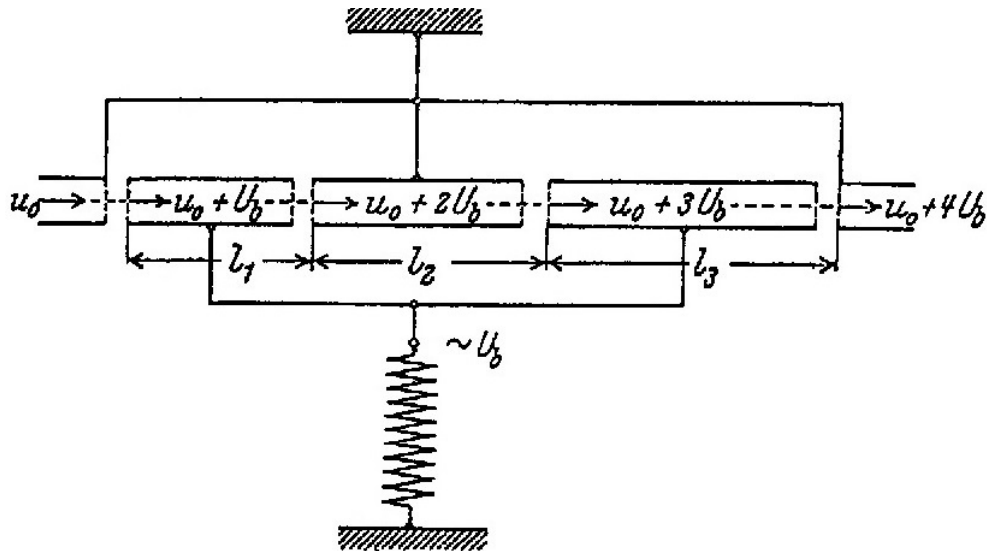
Figure 1.1. Illustration of Wideroe's Accelerator (Source: Wideroe, 1928)

The invention of RF accelerators would also be the key to the rise to higher acceleration gradients. For instance, more than 13-meter-high Van de Graaff generator (Van de

Graaff et al., 1933), which was developed in late 20s and early 30s, could rise to very high voltages. However, as a basic concern for an accelerator is to decrease the length of the accelerating path since the shorter the distance at constant voltage, the higher the obtained electric field and the acceleration gradient. On the other hand, one of the main problems of this generator was to discharge its load to the ground due to ionization of air when trying to reach higher voltages. Kilpatrick criterion, an empirical touchstone obtained for copper, showed that higher electric field levels could be seen without arc as higher frequencies were reached (Kilpatrick, 1957), see Equation 1.1 and Figure 1.2.

$$f(MHz) = 1.64e^{\left(\frac{-17}{2|\vec{E}|}\right)}|\vec{E}|^2 \tag{1.1}$$

where the unit of the electric field value, $\vec{E}$, is MV/m and f stands for the source frequency. The coefficients of the empirical equation is not valid anymore because copper was not as pure as today, but the behaviour is the same (Chao and Tigner, 1999; Wangler, 1998; Bahng et al., 2017). One can easily conclude that the higher the frequency, the higher the voltage in the same distance.
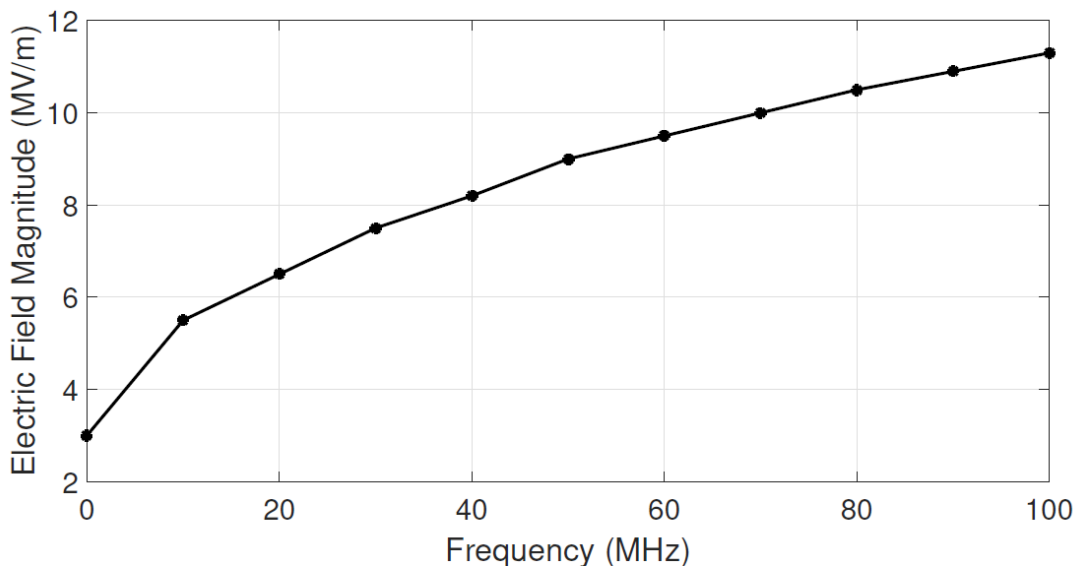
Figure 1.2. Kilpatrick Limit

In 1938, the resonator cavity concept that is one of the most important steps in the history of accelerator was developed (Hansen, 1938; Nassiri et al., 2016). In addition to

mathematical inference of rectangular, cylindrical and spherical resonators, it gave us a clear idea of the applicability of the TM_{01x} mode used in the accelerator cavities today. Shortly after Hansen's publication, klystron, an amplifier capable of increasing RF energy to high levels, was invented (Varian and Varian, 1939) and this allows higher powers to be achieved. In 1948, Alvarez type linear accelerator was developed due to electromagnetic wave emission of drift tube accelerators. This linear accelerator contained drift tubes placed inside a cavity, and could prevent electromagnetic emission. After the end of the World War II, in the early 50s, with the rise of high power needs, klystrons started to used in accelerators (Chodorow et al., 1953) and compared to the magnetron oscillators that are used before the klystrons, much higher energy levels could be achieved in the accelerator structures.

After the power supplies were sufficiently strengthened, the losses on the cavity walls became a major problem. Bringing the surface resistance of the cavity walls to zero was the key to keeping power lost to heat as few as possible, so a superconducting proton linac was proposed in the early 60s (Banford and Stafford, 1961) and a superconducting linear accelerator was fabricated at Stanford University in almost the same years (Wilson et al., 1963). With the introduction of superconductor technology into accelerator systems, energy levels have increased rapidly, and in the early 2000s in an experiment at CERN, the energy of the particles has been increased to above 100 GeV (Brown et al., 2001).

Today, there are thousands of particle accelerators in the world, and they are used in many areas such as medical applications, isotope production, high energy physics etc. (Padamsee, 2017). These structures can be divided into two main groups: linear and circular. Linear accelerators, like RFQ, Drift Tube Linac etc., can be used only once by each particle bunch, while particles can pass through circular accelerators multiple times. Linear accelerators are generally used to strike the particles to a fixed target, especially in medical applications. On the other hand, a higher particle energy can be achieved with circular accelerators and higher energy collision experiments can be performed. More than 40% of the particle accelerators in the world are used in medical applications, while less than 1% are used for high energy physics (Cuttone, 2008).

1.1. Overview of Elliptical Cavities

Many of the modern particle accelerators use accelerating cavities to accelerate particle bunches. There are numerous and different types of accelerator cavities, and as

time goes by, new designs are proposed. Basically, the cavities hold the electric and magnetic fields inside them and the patterns they form are called modes. It is worth to mention the meaning of the mode names which will be mathematically derived in the next chapter.

- TM: $H_z = 0, E_z \neq 0$

- TE: $H_z \neq 0, E_z = 0$

- TEM: $H_z = 0, E_z = 0$

where the propagation direction is $\vec{z}$ (Pozar, 2005).

The direction of motion of the particle and the direction of the electric field must be the same inside of the cavities, see Equation 1.2. Moreover, the magnetic field cannot be used to accelerate charged particles, since the result of the cross product in Equation 1.2 is orthogonal to $\vec{v}$. Therefore, the electric field is used to accelerate particle beams, while the magnetic field is used to bend or focus them.

$$\vec{F} = q_a \vec{E} + q_a \vec{v} \times \vec{B} \tag{1.2}$$

where $\vec{v}$ denotes the velocity of the particle and q_a stands for the charge of the considered particle.

For low and medium-β particles, where β means the the particle speed normalized to the speed of light, cavities such as Spoke Cavity, Half-Wave and Quarter-Wave resonators that accelerate with TEM mode can be used (Delayen, 2010). On the other hand, RFQ, which is capable of both acceleration and focusing at lower speeds, is also a frequently encountered accelerator cavity for accelerator systems (Hansborough et al., 1981). As the particles reach higher velocities, elliptical cavities begin to emerge. These standing wave structures, that are often fabricated as superconductors and designed to accelerate high-β particles, generally provide acceleration with TM mode. These cavities are basically derived from the pillbox cavity structure and use TM_{010} mode for acceleration. Since the non-smooth portions of the pillbox cavity are quite large, there has been a need to smooth out those regions. That's why pillbox cavities are generally not preferred for acceleration because the probability of multipacting increases due to sharp edges (Nassiri et al., 2016). An elliptical cavity may be single cell or multicell depending on the application. The famous 9-cell TESLA cavity operating at 1.3 GHz can be seen in Figure 1.3.

Figure 1.3. 9-Cell Elliptical Cavity (Source:Vostrikov, 2015)

The elliptical cavities usually perform acceleration with a special mode, called the π-mode (Juntong, 2011), see Figure 1.4. First, the particle enters the cavity from the left, while the direction of the electric field in the first cell is from left to right. After half a period, the direction of the electric field reverses but the particle has already entered the second cell. Thus, the particle is accelerated continuously and this acceleration mode is called π-mode due to the phase difference between the cells. If the electric field directions in all cells were the same at the same time, then they would be called zero-mode. In zero-mode, the peak electric field value of the middle cells can go to high levels, while the electric field magnitude in the end cells is lower.
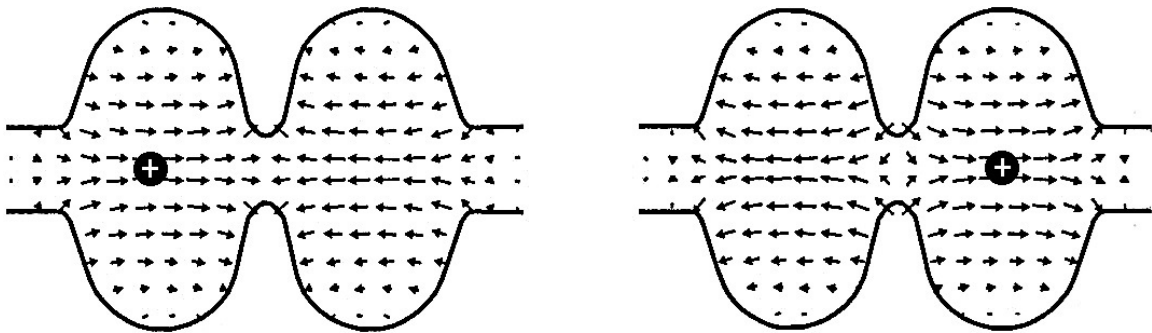

Figure 1.4. Representation of π-mode for a Two-cell Elliptical Cavity

1.2. Literature Search and Motivation

Particle accelerators and accelerator cavities need highly sophisticated design processes and their construction is very expensive. Especially the superconducting accelerator cavities start to be used after very precise and expensive production and testing.

However, unavoidable errors occur in these fabricated cavities. At this point, it is the most rational path to make arrangements to minimize the undesired effects. Generally speaking, if we cannot prevent the faulty fabrication of the structure, examining the effect of the error and eliminating these problems with different methods has an important place in the accelerator field as well as in all areas.

Modeling faults or observing possible consequences of the specific effects has been an interesting topic in this field for years. Investigation of surface roughness and different manufacturing defects is very important not only for accelerator cavities, but also for various kinds of RF equipment. In this context, different types of methodologies have been developed for different structures to reduce the computer simulation time or to understand the consequences of possible fabrication errors. For instance, empirical (Hammerstad and Jensen, 1980) or scattering-based models (Huray et al., 2007; Hall et al., 2007; Huray et al., 2010) related to microstrip lines have been proposed and the effects of surface roughness of microstrip lines can be examined more easily. In time, improved versions of these models have also been developed and major advances have been made in the field of computer-aided microwave design (Simonovich, 2016). Apart from microstrip lines, many studies have been conducted to examine the effects of surface roughness on waveguides and cavities. Some of these studies model waveguides and losses caused by surface roughness on a lumped circuit (Lomakin et al., 2017; Lomakin et al., 2018), while the others obtained a surface impedance by obtaining full Maxwell solutions on rough and smooth surfaces (Gold and Helmreich, 2015).

Not only the surface roughness but also the examination of different fabrication errors have important places in the literature. For instance, there are numerous studies for TESLA cavities that examine for the cases of incorrect fabrication of the cell's length, radius, or circular shape and develops a method to model this situation (Sulimov et al., 2013; Xiao et al., 2007; Akcelik et al., 2008). Furthermore, frequency shift due to the force applied during the equator connection of an elliptical cavity is examined in a separate study (Sulimov, 2015). Also, the effect of the errors that occur during deep drawing and electron beam welding on resonant frequency and field flatness observed experimentally in JLAB can be found in the literature (Marhauser, 2011).

In this thesis, in addition to these studies, electromagnetic problems caused by possible misalignment during equator welding and possible solutions of some of these problems are examined. The fabrication of the elliptical accelerator cavities is based on the formation of half-cells by shaping niobium sheets in various ways, see Figure 1.5. After half-cells are manufactured, they are bonded together by electron beam welding

(Zhao et al., 2007; Saha et al., 2012). At this point, alignment error on the equator of individual cells is inevitable, albeit very small (Olry and Leluan, 2001). Even if it is actually at the micrometer level or if different fabrication errors dominate the alignment error, it may be important to investigate the effects of individual alignment errors in future projects.

(a)   (b)

Figure 1.5. Fabricated Mid Dumbbells (a) Cavity at JLAB (b) TESLA Cavity (Source: Delayen, 2008)

The manufactured structures are generally used as superconductors under 4 Kelvin (Singer, 2017). Normal conductive elliptic cavities are also used in some facilities (Xiao et al., 2015), while their fabrication processes may vary depending on the material used. For example, when fabricating an aluminum structure, the inside of the cells can be carved with a CNC or similar engraving tool. In this case, surface roughness is quite possible and even if surface treatment is performed, it is not possible to completely get rid of this roughness. It is necessary to examine the electromagnetic effects of not only cell misalignment, but also possible surface roughness, particularly for normal conductive structures in this thesis.

CHAPTER 2

THEORETICAL BACKGROUND

In this chapter, numerical methods and models used in the thesis and some background information related to accelerator cavity structures will be given.

2.1. Numerical Approaches for Accelerator Cavity Simulations

There are various 2D or 3D programs used in microwave device design where some of those are commercial and some of them are freely downloadable. For instance, by considering 3D commercial software CST Studio Suite and Ansys HFSS are the most preferred programs in this area. On the other hand, openEMS, an open source code, which provides 3D solutions of the Maxwell's equations with the aid of FDTD method (Liebig et al., 2013), and Superfish, which finds 2D solutions and applies the solution to three-dimensional objects using cylindrical symmetry (Halbach and Holsinger, 1976), also have a very important place. In addition, MAFIA, a 3D electromagnetic simulator, is a frequently used program in accelerator community (Ebeling et al., 1989). It is also worth that, ADS, AWR, Cadence programs are also commonly used programs. In this thesis, cavity design and some other electromagnetic simulations were performed by using Microwave Studio of CST program.

2.1.1. CST-MWS Software for Eigenvalue and Wake Simulations

The CST-MWS is an electromagnetic simulation program that incorporates several numerical solution methods like finite element method, finite integration method etc. Throughout this study, 3 different numerical solvers, i.e. E-solver, frequency domain solver and wakefield solver have been used. While the E-Solver of the CST software can be used for cavity design, frequency domain solver can be employed in the calculation of S-parameters, and wakefield solver can be utilized to calculate the wakefields and impedances in the accelerator cavity.

E-solver treats the electromagnetic problem as an eigenvalue problem and can cal-

culate natural modes of an arbitrarily shaped resonant structure, like in Figure 2.1, without the need of any excitation source. In this problem, electric field is the eigenvector while square of free space wave number corresponds to the eigenvalue, see Equation 2.1. If the structure is lossy, the wavenumber becomes a complex number and the imaginary part is inversely proportional to the quality factor. The program basically divides the desired structure into small meshes and solves it numerically. In the E-solver of the program, there are two different meshing methods, tetrahedral and hexahedral.
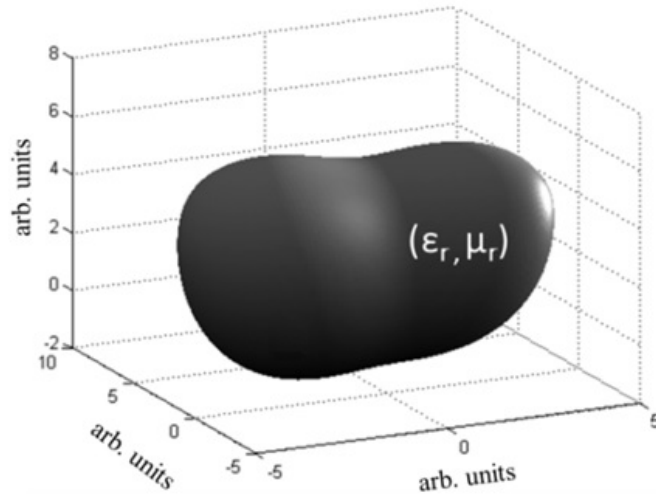
Figure 2.1. Arbitrary Resonant Cavity Structure (Source:Karatay and Yaman, 2019a)

$$\left(\frac{1}{\mu_r\mu}\right)\nabla \times \nabla \times \vec{E} = \omega^2\epsilon_r\epsilon\vec{E} \qquad (2.1)$$

where ω is angular frequency, μ indicates magnetic permeability, μ_r stands for relative magnetic permeability, ϵ and ϵ_r denote electric permittivity and relative electric permittivity, respectively.

On the other hand, when the cavity is excited, reflection and transmission plots of the electromagnetic wave for different frequency samples may be desired. For this, it is necessary to use the frequency domain solver that solves problems in phasor form, see Equation 2.2.

$$\vec{E}(\vec{r}, t) = Re\{\vec{E}(\vec{r}, \omega)e^{j\omega t}\} \qquad (2.2)$$

where $\vec{r}$ symbolizes 3x1 vector that contains spatial coordinates.

Unlike E-solver, at least one excitation source is required in the frequency domain solver, and these excitation sources are generally defined as discrete or waveguide ports of a cavity excitation simulation. This enables the S-matrix, whose definition can be seen in Equation 2.3, of the respective microwave network to be obtained. Alternatively, field source options instead of excitation source can be used in high frequency simulations. This solver evaluates the Maxwell's equation system for individual frequency samples, and uses an adaptive algorithm to obtain only the frequency samples that are chosen.

$$S = \begin{bmatrix} s_{11} & s_{12} & \cdots & s_{1n} \\ s_{21} & s_{22} & \cdots & s_{2n} \\ \cdots\cdots\cdots\cdots\cdots\cdots \\ s_{n1} & s_{n2} & \cdots & s_{nn} \end{bmatrix}_{nxn} \quad where\ s_{mp} = \left.\frac{V_m^-}{V_p^+}\right|_{V_k=0},\ k \neq p \qquad (2.3)$$

- If m=p, s_{mp} means reflection at the pth port.

- If m≠p, s_{mp} means transmission from the pth port to the mth port.
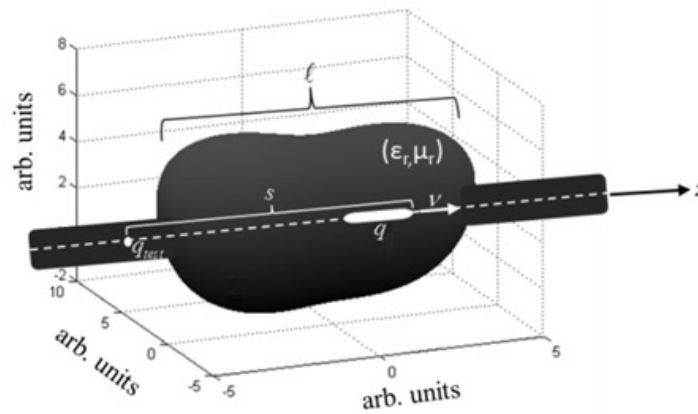
Figure 2.2. Wake Field Simulation Scenario (Source: Karatay and Yaman, 2019a)

In addition to the mentioned solvers, simulations were also performed with wakefield solver. The wakefield solver of the CST program is capable of calculating parameters such as wake potential, wake impedance and wake function which can be basically con-

sidered as electromagnetic field residues left behind by moving charged particles, called as bunch.

Consider a leading bunch traveling inside an arbitrarily shaped cavity and a following test particle with a charges of q and q_{test}, respectively. Lorentz force on the test particle is written as,

$$\vec{F}(\vec{r}, t) = q_{test}\vec{E}(\vec{r}, t) + q_{test}\vec{v} \times \vec{B}(\vec{r}, t) \qquad (2.4)$$

Since we are only interested in the longitudinal component in this study, the equation is reduced.

$$F_{||}(\vec{r}, t) = q_{test}E_z(\vec{r}, t) \; where \; x, y = 0 \qquad (2.5)$$

The energy gain of the test particle is equal to the line integral of the force acting on it.

$$U_{||}(s) = \int_0^l \mathrm{d}z F_{||}(z, t)\Big|_{t=\frac{s+z}{v}} \qquad (2.6)$$

Longitudinal wake function, $w_{||}$(s), is obtained by normalizing the minus sign of energy gain to q_{test} times q while the longitudinal length of the leading bunch is considered approximately zero (Novokhatski, 2012). Also, wake impedance, $Z(\omega)$ is the Fourier transform of the wake function (Zotter and Kheifets, 1998). As can be followed, the convolution of the normalized line charge density, ρ_l, and the longitudinal wake function gives us the longitudinal wake potential (Novokhatski and Mosnier, 2014).

$$W_{||}(s) = \int_0^l \mathrm{d}\tau w_{||}(\tau)\rho_l(s - \tau) \qquad (2.7)$$

In some sources, the convolution of charge density and wake function is calculated without normalization and the unit of longitudinal wake potential is found as V (Palumbo

et al., 1994), but this value is generally used as a normalized value and the unit is V/C (Tsakanian et al., 2011; Fujita et al., 2006; Fujita et al., 2009).

2.1.2. Surface Impedance Models in CST Software

Suppose that effects of roughness on a metal surface is desired to be simulated. Depending on the variation of the roughness, the time and CPU power required to solve this metal's characteristic can be very large. Therefore, it is wise to express the conductivity of that metal as a complex number and shorten the simulation time, significantly. The CST software offers two main models: Hammerstad-Jensen and Huray's snowball, and both models are mainly developed for microstrip lines.

2.1.2.1. Hammerstad-Jensen Model

Microstrip lines are highly complex structures to solve analytically that support quasi-TEM modes. In particular, the analytical solution of the surface roughness to be added to these structures is even more laborious. For this reason, empirical models are frequently used. In this context, the main purpose is to express the surface impedance and thus the power loss as a function depending on the surface roughness. The Hammerstad-Jensen model proposes us the following empirical formula, see Equation 2.8 (Hammerstad and Jensen, 1980).

$$Z_s\left(\Delta_{rms}\right) = Z_s\left(0\right)\left(1 + \frac{2}{\pi}\left[tan^{-1}\left(\frac{7\Delta_{rms}^2}{5\delta^2}\right)\right]\right) \tag{2.8}$$

where Z_s represents surface impedance, Δ_{rms} and δ stand for RMS amplitude of the surface roughness and penetration depth, respectively.

2.1.2.2. Huray's Model

A more accurate model is needed because the Hammerstad-Jensen model shifts away from actual values at high frequencies. In particular, the insertion loss values above

5 GHz begin to be different. The Huray model defines the roughness on the microstrip line as a large number of spheres and performs its analysis in this context (Huray et al., 2007; Hall et al., 2007). Therefore, this model is also called Huray's snowball model. When looking at the SEM images, it can be said that the snowball model looks much closer to the actual roughness images (Huray et al., 2010). The normalized power loss formula proposed by the Huray snowball model can be seen in Equation 2.9. Note that, the following formula does not take into account some resonance points occurring above 30 GHz.

$$\frac{P_{rough}}{P_{smooth}} = 1 + 1.5 \left(\frac{K 4 \pi r_s^2}{H \left(1 + \frac{\delta}{r_s} + \frac{\delta^2}{2 r_s^2} \right)} \right) \tag{2.9}$$

where K stands for number of spheres, r_s is radius of spheres, H represents hexagonal area and δ indicates penetration depth. Note that, this formula is in fact an iterative formula, but only the result of the first iteration is given in Equation 2.9. If the result does not converge as it is expected, then the radii and the total number of spheres are updated iteratively. We note that, it has been shown previously that this model can be used for a resonator structure even at THz frequencies (Fawole and Tabib-Azar, 2016).

2.2. Electromagnetic Field Distributions in Cavities

A cavity is a resonator structure obtained by short-circuiting ends of a waveguide or using a metal box. Since the ends of the waveguide are short-circuited, an impedance mismatch occurs and a standing wave pattern is generated. The wavelength and the dimensions of the cavity must be proportional to create a resonance within the cavities. For example, in a rectangular cavity, the dimensions of the cavity should be multiples of half a wavelength for non-zero modes (Pozar, 2005). In theory, an infinite number of modes can be excited in a cavity and each mode has a different electromagnetic pattern. Depending on the direction and number of repetitions of the electric and magnetic fields in these patterns, each mode is called with a specific name. If there is no electric field component in the propagation direction of electromagnetic wave, such modes are called TE mode. Similarly, if there is no magnetic field component in the direction of propagation, then such modes are called TM mode. If there is neither electric nor magnetic field in propagation direction, that kind of mode is called TEM mode. TEM modes cannot be excited

in rectangular, cylindrical, elliptical types of cavities unless there is a metallic object in the middle of the cavity. TM mode, mostly TM_{010}, is used for acceleration in the pillbox and elliptical accelerator cavities.

The mathematical expressions of modes for a cylindrical cavity are derived in the following subsections. Note that, the propagation direction is assumed to be $\hat{z}$.

2.2.1. TM Modes

Scalar Helmholtz equation is satisfied by magnetic vector potential, $\vec{A}$, and it has only component that is $A_z \hat{z}$.

$$\Delta A_z + k_{mnp}^2 A_z = 0 \tag{2.10}$$

Assume $A_z = R(\rho)F(\phi)Z(z)$. If Laplacian term in Equation 2.10 is expanded in cylindrical coordinates, and all terms are divided by $R(\rho)P(\phi)Z(z)$,

$$\frac{1}{\rho R(\rho)}\frac{\mathrm{d}}{\mathrm{d}\rho}\left(\rho\frac{\mathrm{d}R(\rho)}{\mathrm{d}\rho}\right) + \frac{1}{\rho^2 P(\phi)}\frac{\mathrm{d}^2 P(\phi)}{\mathrm{d}\phi^2} + \frac{1}{Z(z)}\frac{\mathrm{d}^2 Z(z)}{\mathrm{d}z^2} + k_{mnp}^2 = 0 \tag{2.11}$$

$$\frac{1}{\rho R(\rho)}\frac{\mathrm{d}}{\mathrm{d}\rho}\left(\rho\frac{\mathrm{d}R(\rho)}{\mathrm{d}\rho}\right) + \frac{1}{\rho^2 F(\phi)}\frac{\mathrm{d}^2 P(\phi)}{\mathrm{d}\phi^2} - k_z^2 + k_{mnp}^2 = 0 \tag{2.12}$$

Now, both sides of the equation are multiplied by ρ^2 to make the second term in Equation 2.12 depend on only ϕ. Then the equation can be written in the following form.

$$\frac{\rho}{R(\rho)}\frac{\mathrm{d}}{\mathrm{d}\rho}\left(\rho\frac{\mathrm{d}R(\rho)}{\mathrm{d}\rho}\right) - m^2 + \rho^2(k_{mnp}^2 - k_z^2) = 0 \tag{2.13}$$

Lastly, both sides of the equation are multiplied by $R(\rho)$, and $\left(k_{mnp}^2 - k_z^2\right)$ is replaced with k_ρ^2. Bessel differential equation can be seen in Equation 2.14.

$$\rho\frac{\mathrm{d}}{\mathrm{d}\rho}\left(\rho\frac{\mathrm{d}R(\rho)}{\mathrm{d}\rho}\right) + \left((\rho k_\rho)^2 - m^2\right)R(\rho) = 0 \tag{2.14}$$

The solution of the differential equation given in Equation 2.14 corresponds to Bessel functions of the first kind, since the magnitude of the electric field at the center of the cavity is finite. The resultant expression for A_z of TM modes in cylindrical cavities can be written as follow:

$$A_z = (A sin(m\phi) + B cos(m\phi)) \, J_m(k_\rho \rho)(C cos(k_z z) + D sin(k_z z)) \qquad (2.15)$$

where A, B, C and D are arbitrary constants.

It is known that $\vec{E} = -jw\vec{A} + \frac{1}{j\omega\epsilon\mu}\nabla(\nabla \cdot \vec{A})$ and $\vec{H} = \frac{1}{\mu}\nabla \times \vec{A}$, then one can write the field expressions easily. Applying the boundary condition, derivative of A_z must be equal to 0 at z=0 and z=h, D is found to be zero. In this case the constant C is substituted into the new constants F_{mnp} and G_{mnp}.

$$E_\rho = \frac{jk_\rho k_z}{\omega\mu\epsilon} (F_{mnp} sin(m\phi) + G_{mnp} cos(m\phi)) \, J'_m(k_\rho \rho) sin(k_z z) \qquad (2.16)$$

$$E_\phi = \frac{jmk_z}{\omega\mu\epsilon\rho} (F_{mnp} cos(m\phi) - G_{mnp} sin(m\phi)) \, J_m(k_\rho \rho) sin(k_z z) \qquad (2.17)$$

$$E_z = \frac{-j(\omega^2\mu\epsilon - k_z^2)}{\omega\mu\epsilon} (F_{mnp} sin(m\phi) + G_{mnp} cos(m\phi)) \, J_m(k_\rho \rho) cos(k_z z) \qquad (2.18)$$

$$H_\rho = \frac{m}{\mu\rho} (F_{mnp} cos(m\phi) - G_{mnp} sin(m\phi)) \, J_m(k_\rho \rho) cos(k_z z) \qquad (2.19)$$

$$H_\phi = \frac{-k_\rho}{\mu} (F_{mnp} sin(m\phi) + G_{mnp} cos(m\phi)) \, J'_m(k_\rho \rho) cos(k_z z) \qquad (2.20)$$

$$H_z = 0 \qquad (2.21)$$

where $k_z = \frac{p\pi}{h}$ and $k_\rho = \frac{\chi_{mn}}{r}$.

The fundamental acceleration mode for a pillbox cavity is TM$_{010}$. Specifically, if the field distributions for the TM$_{010}$ mode are written, all components containing $\sin(k_z z)$ terms will be zero. On the other hand, if there is an "m" coefficient at the beginning of the expression, the corresponding component will be equal to 0 again.

$$E_\rho = E_\phi = H_\rho = H_z = 0 \tag{2.22}$$

$$E_z = \frac{-jG_{010}k^2}{\omega\mu\epsilon}J_0(k_\rho\rho) = E_{010}J_0(\frac{2.405\rho}{r}) \tag{2.23}$$

$$H_\phi = \frac{-G_{010}k_\rho}{\mu}J_0'(k_\rho\rho) = H_{010}J_1(\frac{2.405\rho}{r}) \tag{2.24}$$

where E$_{010}$ and H$_{010}$, with units of V/m and A/m respectively, depend on input power, and 2.405 means the first root of Bessel function of the first kind in the zeroth order.

As seen in Equations 2.23-2.24, TM$_{010}$ mode has no longitudinal and angular dependence, and only the longitudinal component of the electric field exists.

2.2.2. TE Modes

In TE mode, as in TM mode, the solution is obtained by using the seperation of variables method. However, in this mode, the electric vector potential, $\vec{Y}$, is used instead of the magnetic vector potential. The relationship between the electric vector potential and the electric and magnetic field can be seen in Equations 2.25 and 2.26.

$$\vec{H} = -jw\vec{Y} - \frac{1}{j\omega\epsilon\mu}\nabla(\nabla \cdot \vec{Y}) \tag{2.25}$$

$$\vec{E} = -\frac{1}{\epsilon}\nabla \times \vec{Y} \tag{2.26}$$

16

Just as in TM mode, the electric vector potential also contains only $\hat{z}$ component, which must satisfy the Helmholtz equation, see Equation 2.10. The general solution is also obtained for TE modes with the separation of variables method. Field components are found by performing the same operations as TM modes. At last, the electric field component in the direction of the wave propagating is zero. Derivation procedures of Y_z can be found in a wide variety of books (Balanis, 1989; Hill, 2009). The field components for TE mode of a cylindrical cavity can be seen in the following.

$$H_\rho = \frac{-jk_\rho k_z}{\omega\mu\epsilon} \left(K_{mnp}cos(m\phi) + L_{mnp}sin(m\phi)\right) J'_m(k_\rho\rho)cos(k_z z) \tag{2.27}$$

$$H_\phi = \frac{jmk_z}{\omega\mu\epsilon\rho} \left(K_{mnp}sin(m\phi) - L_{mnp}cos(m\phi)\right) J_m(k_\rho\rho)cos(k_z z) \tag{2.28}$$

$$H_z = \frac{-j(\omega^2\mu\epsilon - k_z^2)}{\omega\mu\epsilon} \left(K_{mnp}cos(m\phi) + L_{mnp}sin(m\phi)\right) J_m(k_\rho\rho)sin(k_z z) \tag{2.29}$$

$$E_\rho = \frac{m}{\mu\epsilon} \left(K_{mnp}sin(m\phi) - L_{mnp}cos(m\phi)\right) J_m(k_\rho\rho)sin(k_z z) \tag{2.30}$$

$$E_\phi = \frac{k_\rho}{\epsilon} \left(K_{mnp}cos(m\phi) + L_{mnp}sin(m\phi)\right) J'_m(k_\rho\rho)sin(k_z z) \tag{2.31}$$

$$E_z = 0 \tag{2.32}$$

where K_{mnp} and L_{mnp} are the arbitrary constants depending on the input power.

2.3. Fundamental Accelerating Cavity Parameters

There are various parameters that should be optimized to obtain an efficient acceleration. In this section, those parameters will be introduced.

2.3.1. Resonant Frequency

Resonant frequency of a specific mode is one of the most important parameter of a cavity structure. The oscillation frequency of the power supply and the demanded resonant frequency of the cavity mode must be matched so that the incident power can be transferred into the cavity. Resonant frequency of a cylindrical cavity can be seen in Equations 2.33.

$$f_{mnp} = \frac{c}{2\pi\sqrt{\epsilon_r \mu_r}}\sqrt{\left(\frac{\chi_{mn}}{r}\right)^2 + \left(\frac{p\pi}{h}\right)^2} \tag{2.33}$$

In Equation 2.33, r and h represents radius and height of a cylindrical cavity, respectively. Also, it should be noted that χ_{mn} stands for the roots of Bessel functions for TM modes and roots of derivative of Bessel functions for TE modes.

In parallel RLC equivalent circuit approach, resonant frequency is expressed as in Equation 2.34.

$$f = \frac{1}{2\pi\sqrt{L_{par}C_{par}}} \tag{2.34}$$

where L_{par} and C_{par} are the inductance and capacitance of the parallel equivalent circuit, respectively.

2.3.2. Accelerating Voltage

This parameter describes the effective voltage seen by the bunch of particles. If the voltage on the beam axis was fixed, then the accelerating voltage would be equal to the applied voltage inside the cavity. However, the particle bunch is exposed to a sinusoidally varied voltage, and the accelerating voltage is less than the peak value of applied voltage due to sinusoidal variation (Wangler, 1998).

$$V_{acc} = \left| \int_0^L E_z(\rho = 0, z)e^{j\frac{\omega}{v_b}z}\mathrm{d}z \right| \tag{2.35}$$

where L is the length of the cavity, ω represents the angular resonant frequency and v_b is the speed of the particle bunch.

2.3.3. Accelerating Gradient

Accelerating gradient is the parameter that describes the accelerating voltage per meter.

$$E_{acc} = \frac{V_{acc}}{L} \tag{2.36}$$

Only the acceleration gradient parameter does not give sufficient information on the characteristics of a cavity. Peak surface electric field (PSEF) and peak surface magnetic flux density (PSMFD) normalized to accelerating gradient give us insight to the quality of the cavity and provide material independent parameters that should be optimized.

2.3.3.1. Normalized PSEF

This parameter is the ratio between PSEF that occurs around iris region and accelerating gradient. It is one of the material invariant cavity parameters, and should be minimized to avoid electron emissions in superconducting structures. Since the numerator and denominator have the same unit, the term is unitless and the typical value of E_{peak}/E_{acc} is around 2-3 for an elliptical cavity. On the other hand, this value is equal to 1.57 for a smooth pillbox cavity (Ebeling et al., 1989).

2.3.3.2. Normalized PSMFD

This parameter is the ratio between PSMFD that occurs around equator region and accelerating gradient. It should be minimized to avoid superconductivity breakdown. The unit of the numerator is Tesla and the unit of denominator is V/m and the typical value of B_{peak}/E_{acc} is around 4-5 mT/(MV/m). Normalized PSMFD in an ideal pillbox cavity is 3.05 mT/(MV/m) (Ebeling et al., 1989).

2.3.4. Quality Factor

Quality factor is one of the most important parameters in determining the power capacity that a cavity can hold. Basically, it is proportional to the square root of the conductivity of the cavity walls as well as the shape of the cavity. One can calculate the quality factor of an arbitrary cavity with the aid of Equation 2.37.

$$Q = \frac{2\pi f \mu \int_V |\vec{H}|^2 dv}{R_s \oint_S |\vec{H}_{\tan}|^2 ds} = 2\pi \frac{Energy\ Stored\ Inside\ the\ Cavity}{Period * Power\ Dissipated\ in\ Each\ Cycle} \qquad (2.37)$$

where the formulation of surface resistance, R_s can be found as follows,

$$R_s = \sqrt{\frac{\pi f \mu}{\sigma}} \qquad (2.38)$$

where σ denotes the bulk conductivity of the material.

Clearly, if the electromagnetic field pattern in the cavity is known, then the quality factor can be calculated analytically. Specifically, field distributions of a pillbox cavity are associated with Bessel functions, so the volume and surface integrals of Bessel functions give exact value of quality factor of a pillbox cavity. Very simple form of the quality factor of TM$_{010}$ mode of a pillbox cavity is

$$Q_{010(pillbox)} = \frac{2\pi f h r \mu \sqrt{\sigma}}{2\sqrt{\pi f \mu}(r+h)} = \sqrt{\pi f \mu \sigma} \left(\frac{hr}{h+r} \right) \qquad (2.39)$$

The quality factor in Equation 2.39 is based on the assumption that the inside of the cavity is not filled with a lossy dielectric, otherwise dielectric losses in the cavity must be taken into account. However the dielectric loss can be ignored since the accelerator cavities are generally operating in vacuum conditions.

While it is possible to analytically or numerically find the Q value of a cavity, the experimental measurement requires post-processing. It is practically impossible to directly measure the quality factor of a cavity since the cavity will certainly be coupled to the circuitry of measuring instruments or different external circuits. In this case, the

measured quality factor value is the total Q value of the whole system. It is necessary to know how much the cavity is coupled to the external circuit in order to extract the cavity's own quality factor from the measured value. The relationship between the coupling factor and quality factor can be seen in Equations 2.40 and 2.41.

$$Coupling\ Factor\ (CF) = \frac{Q_0}{Q_{external}} = \frac{S_{21}}{1 - S_{21}} \tag{2.40}$$

$$\frac{1}{Q_{loaded}} = \frac{1}{Q_0} + \frac{1}{Q_{external}} = \frac{1 + CF}{Q_0} \tag{2.41}$$

where Q_{loaded} is the measured value of quality factor, Q_0 represents the unloaded quality factor of the cavity, $Q_{external}$ stands for the quality factor of external circuitry and S_{21} is insertion loss of the 2-port network.

If the coupling is weak enough, the external quality factor can be omitted and the loaded quality factor is equal to the unloaded quality factor in this case. Accordingly, one can measure the unloaded quality factor via 2-port VNA measurement. The loaded quality factor, on the other hand, is the ratio of the resonant frequency and bandwidth, see Equation 2.42.

$$Q_{loaded} = \frac{f_0}{\Delta f} \tag{2.42}$$

where $\Delta f = f_{-3dB}^{high} - f_{-3dB}^{low}$.

Alternatively, one can find the quality factor of a cavity with one-port measurement. Since it is not possible to find the -3 dB points by looking at the S_{11} plot in weak coupling, one should adjust the coupling factor to 1, and multiplies the measured value by 2 to obtain the unloaded quality factor, see 2.41. The relationship between the coupling factor and S_{11} can be seen in Equation 2.43.

$$S_{11} = \frac{CF - 1}{CF + 1} \tag{2.43}$$

Suppose the cavity is expressed as an equivalent parallel RLC circuit. In this case, Q is expressed as in Equation 2.44.

21

$$Q = 2\pi f R_{par} C_{par} \tag{2.44}$$

where R_{par} denotes the resistance and C_{par} indicates the capacitance of the parallel equivalent circuit of a cavity.

2.3.5. Geometry Factor

Geometry factor (or geometric factor) is material-independent quality factor, see Equation 2.45. In other words, it is obtained by eliminating the surface resistance in Equation 2.37. Therefore it only depends on the shape of the structure. Two cavities made of different materials with the same shape have exactly the same geometry factors, while their quality factors are different.

$$G = R_s Q \tag{2.45}$$

The geometry factor of TM_{010} mode of a pillbox cavity is expected to be in Equation 2.46. We note that, the expression does not contain the conductivity parameter.

$$G_{010(pillbox)} = \pi f \mu \left(\frac{hr}{h + r} \right) \tag{2.46}$$

2.3.6. Shunt Impedance

This term stands for how much acceleration can be achieved with a certain power loss. In other words, shunt impedance is proportional to the square of the effective voltage seen by the particle bunch. It depends on the shape of the cavity and conductivity of the material used (Wangler, 1998).

$$R_{sh} = \frac{V_{acc}^2}{P_{loss}} = \frac{\left| \int_0^L E_z(\rho = 0, z) e^{j\frac{\omega}{v_b}z} \mathrm{d}z \right|^2}{\frac{R_s}{2} \oint_S \left| \vec{H}_{tan} \right|^2 \mathrm{d}s} \tag{2.47}$$

where $\vec{H}_{tan}$ is the tangential component of the magnetic field and R_s is given by Equation 2.38.

Since the expression V_{acc} represents an effective value, the impedance value is calculated as in Equation 2.47. On the other hand, the expression is written as $\frac{V^2}{2P_{loss}}$ for equivalent circuit approach. Therefore, the shunt impedance values to be obtained in the later chapters of the thesis may be larger than the literature with a factor of 2.

2.3.7. Geometric Shunt Impedance

Since the shunt impedance varies depending on the conductivity of the material used, there is a need to produce a term independent of the material. This parameter defines how effective acceleration is carried out in the cavity and does not contain a material-dependent term (Sekutowicz, 2012).

$$\frac{R_{sh}}{Q} = \frac{\left| \int_0^L E_z(\rho = 0, z) e^{\frac{j\omega z}{v}} \mathrm{d}z \right|^2}{\pi f \mu \int_V |\vec{H}|^2 dv} \tag{2.48}$$

2.3.8. Transit Time Factor

When the particle is moving in the cavity, the electric field in which the particle is interacting is not constant, and it varies in time. This situation is expressed mathematically with transit time factor as in Equation 2.49 (Wangler, 1998).

$$TTF = \frac{\int_{-\frac{L}{2}}^{\frac{L}{2}} E_z(\rho = 0, z) cos\left(\frac{2\pi f z}{v_b}\right) \mathrm{d}z}{\int_{-\frac{L}{2}}^{\frac{L}{2}} E_z(\rho = 0, z) \mathrm{d}z} \tag{2.49}$$

Although the name of the parameter is transit time factor, it is unitless. It expresses the reduction rate in energy gains due to the time-dependent change of the electric field, not the time gone by.

2.3.9. Field Flatness

Accelerator cavities, especially elliptic cavities, are often used as multicell, and the acceleration efficiency of the cavity can be increased in this way. However, one should not ignore the challenges that this situation will arise. One of these challenges is to provide the field flatness on the beam axis.
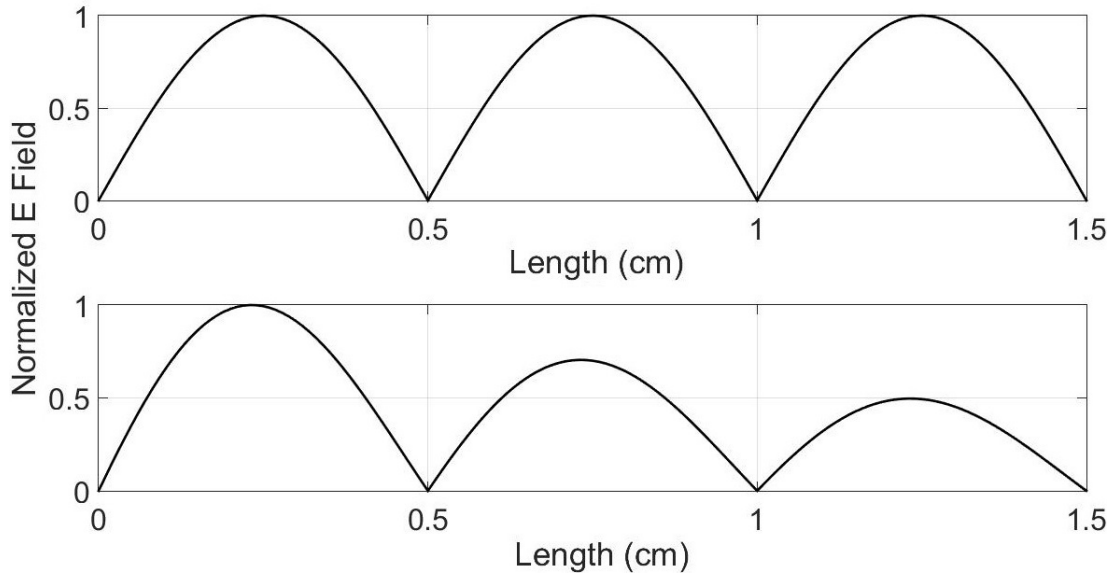
Figure 2.3. Electric Field of 100% (top) and 50% (bottom) Field Flatness

Field flatness refers to the requirement that the maximum value of the electric field in each cell of a multicell cavity is the same. The ratio of the smallest peak electric field and the largest peak electric field is an important parameter that shows the percentage of the field flatness to be achieved (Barbanotti et al., 2010).

$$Field\ Flatness = \frac{|\vec{E}_{peakmin}|}{|\vec{E}_{peakmax}|} \times 100\% \qquad (2.50)$$

In Figure 2.3, each peak refers to the maximum electric field value of a 3-cell elliptical cavity cells on the beam axis. The equalization of the electric field in each cell allows the acceleration gradient to be maximized.

2.3.10. Cell-to-Cell Coupling

Each cell of the multicell elliptic cavities acts as a separate RLC circuit and each cell must be coupled to each other. Depending on whether the coupling is strong or weak, there are some advantages and disadvantages. For instance, as CTCC increases, the distance between neighboring modes increases and geometric variations less affect the fundamental acceleration parameters. On the other hand, the geometric shunt resistance value decreases and therefore more inefficient acceleration occurs.

Suppose, the frequencies between zero-mode and the π-mode of a n-cell elliptical cavity will be measured. In a 2-port measurement, n peaks will be observed, including zero-mode and π-mode. As the CTCC strengthens, these peaks move away from each other or vice versa. The relationship between the CTCC and frequency separation is given in Equation 2.51 (Ebeling et al., 1989).

$$CTCC = \frac{2(f_\pi - f_0)}{f_\pi + f_0} \times 100\% \qquad (2.51)$$

where f_π and f_0 stand for π-mode and zero-mode frequencies of an elliptical cavity, respectively.

2.4. Shape Perturbation

Shape perturbation is a method customized for cavity and waveguides, and provides analytical determination of the results of minor changes in simple structures. Assume a small change is created on a simple structure whose general solution is known. Normally it is not an easy task to solve the new structure analytically, but it is possible to get a rough idea about the new structure based on the unperturbed one. An arbitrarily shaped resonant cavity whose electric and magnetic field distribution is known is considered in Figure 2.4, and it is perturbed with a small defect on the cavity wall that is perfect electrical conductor. The main objective is to find the frequency shift of the cavity which has been perturbed by using the field information of the unperturbed cavity.

Faraday and Ampère equations are written below for both cavities. One should note that the region is source-free, so all source terms are neglected in the equations.
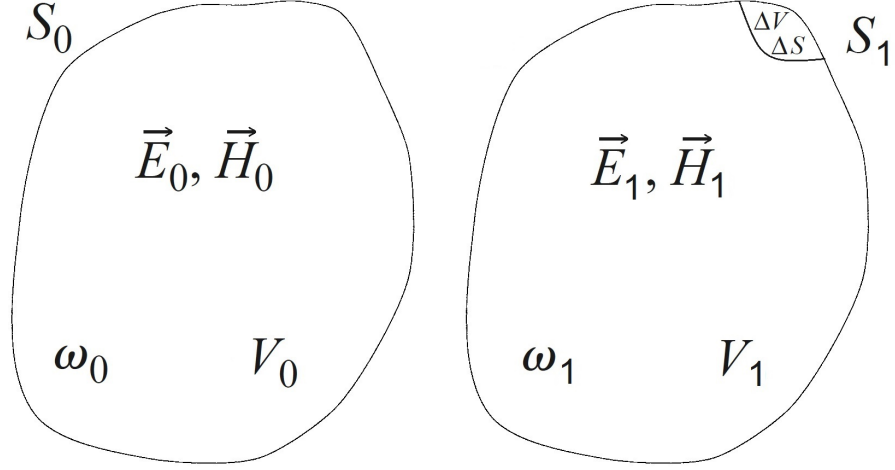
Figure 2.4. Unperturbed and Perturbed Cavities

$$\nabla \times \vec{E}_0 = -j\omega_0\mu\vec{H}_0 \tag{2.52}$$

$$\nabla \times \vec{H}_0 = j\omega_0\epsilon\vec{E}_0 \tag{2.53}$$

$$\nabla \times \vec{E}_1 = -j\omega_1\mu\vec{H}_1 \tag{2.54}$$

$$\nabla \times \vec{H}_1 = j\omega_1\epsilon\vec{E}_1 \tag{2.55}$$

Complex conjugate of Equation 2.52 is multiplied by $\vec{H}_1$ and Equation 2.55 is multiplied by $\vec{E}_0^*$, then they are subtracted each other side by side. Similar operations are applied to Equations 2.53 and 2.54. By using the vector identity given in Equation 2.56, Equations 2.57 and 2.58 can be easily obtained.

$$\vec{X}_1 \cdot (\nabla \times \vec{X}_2) - \vec{X}_2 \cdot (\nabla \times \vec{X}_1) = \nabla \cdot (\vec{X}_2 \times \vec{X}_1) \tag{2.56}$$

26

$$\nabla \cdot (\vec{E}_0^* \times \vec{H}_1) = j\omega_0\mu\vec{H}_1 \cdot \vec{H}_0^* - j\omega_1\epsilon\vec{E}_1 \cdot \vec{E}_0^* \tag{2.57}$$

$$\nabla \cdot (\vec{E}_1 \times \vec{H}_0^*) = -j\omega_1\mu\vec{H}_1 \cdot \vec{H}_0^* + j\omega_0\epsilon\vec{E}_1 \cdot \vec{E}_0^* \tag{2.58}$$

After that, Equations 2.57 and 2.58 are summed, then volume integral is taken over the volume of the perturbed cavity. The volume integral can be turned into a surface integral by using divergence theorem. The resultant equation can be seen in Equation 2.59. Note that, the tangential component of $\vec{E}_1$ is zero on the surface of perturbed cavity.

$$\int_{V_1} \nabla \cdot (\vec{E}_0^* \times \vec{H}_1)\mathrm{d}v + \int_{V_1} \nabla \cdot (\vec{E}_1 \times \vec{H}_0^*)\mathrm{d}v = \oint_{S_1} (\vec{E}_0^* \times \vec{H}_1) \cdot \mathrm{d}\vec{s} + 0 \tag{2.59}$$

The addition of the right-hand sides of Equations 2.57 and 2.58 is written in Equation 2.60.

$$(j\omega_0\mu - j\omega_1\mu)(\vec{H}_1 \cdot \vec{H}_0^*) + (j\omega_0\epsilon - j\omega_1\epsilon)(\vec{E}_1 \cdot \vec{E}_0^*) = j(\omega_0 - \omega_1)(\epsilon\vec{E}_0^* \cdot \vec{E}_1 + \mu\vec{H}_0^* \cdot \vec{H}_1) \tag{2.60}$$

The defect on the cavity wall may be inward or outward. In this case, it can be assumed that $S_1 = S_0 + \Delta S$ or $S_1 = S_0 - \Delta S$ depending on the perturbation on the cavity wall. Assume $S_1 = S_0 - \Delta S$.

$$\oint_{S_0} (\vec{E}_0^* \times \vec{H}_1) \cdot \mathrm{d}\vec{s} - \oint_{\Delta S} (\vec{E}_0^* \times \vec{H}_1) \cdot \mathrm{d}\vec{s} = -\int_{V_1} j(\omega_0 - \omega_1)(\epsilon\vec{E}_0^* \cdot \vec{E}_1 + \mu\vec{H}_0^* \cdot \vec{H}_1)\mathrm{d}v \tag{2.61}$$

where the first integral on the left-hand side is zero since the tangential component of $\vec{E}_0$ is zero on the surface of unperturbed cavity.

Since the main purpose of all these operations is to find the frequency shift, the frequency difference term is left alone in Equation 2.62. If the defect of the cavity surface is assumed to be sufficiently small, the electric and magnetic field distributions of the perturbed cavity can be considered as equal to the unperturbed cavity.

$$\Delta\omega = \frac{\oint_{\Delta S}(\vec{E}_0^* \times \vec{H}_1) \cdot \mathrm{d}\vec{s}}{-\int_{V_1} j(\epsilon\vec{E}_0^* \cdot \vec{E}_1 + \mu\vec{H}_0^* \cdot \vec{H}_1)\mathrm{d}v} \approx \frac{\oint_{\Delta S}(\vec{E}_0^* \times \vec{H}_0) \cdot \mathrm{d}\vec{s}}{-\int_{V_0} j(\epsilon|\vec{E}_0|^2 + \mu|\vec{H}_0|^2)\mathrm{d}v} \qquad (2.62)$$

where $\Delta\omega = \omega_0 - \omega_1$. In other words, when $\Delta\omega$ is positive, this means that the frequency decreases. If Equation 2.57 is substituted into Equation 2.62, one can obtain the normalized frequency shift as follows (Harrington, 1961).

$$\frac{\Delta\omega}{\omega_0} \approx \frac{\int_{\Delta V}(\epsilon|\vec{E}_0|^2 - \mu|\vec{H}_0|^2)\mathrm{d}v}{\int_{V_0}(\mu|\vec{H}_0|^2 + \epsilon|\vec{E}_0|^2)\mathrm{d}v} \qquad (2.63)$$

Note that, the sign of terms in the numerator is related to whether the defect on the cavity wall is inward or outward, and a minus sign may be found at the beginning of the equation in a different notation. In this notation, the outward defect was considered to be positive whereas the inward defect was considered negative. If $S_1 = S_0 + \Delta S$ was assumed in Equation 2.61, then the order of the terms in the numerator of Equation 2.63 would be inverted (Spielman, 2006).

Specifically, the shape perturbation method for TM_{010} mode can be carried out as follows. Suppose that, an inward defect has occurred with the volume of V_r on the side wall of a cylindrical cavity whose inner radius and height are represented with r and h, respectively. The denominator of Equation 2.63 for TM_{010} mode of a pillbox cavity is already known (Pozar, 2005). On the other hand, the volume integral in the numerator should also be calculated while the defect volume is very small compared to the cavity and the field distribution is almost constant in the defect. Furthermore, since the electric field of the TM_{010} mode is approximately zero near to the side wall of a pillbox cavity, only the magnetic field must be integrated.

$$\frac{\Delta\omega}{\omega_0} \approx \frac{\frac{\epsilon}{4}\int_{\Delta V}\left(J_1\left(\frac{2.405\rho}{r}\right)\right)^2 \mathrm{d}v}{0.269475\left(\frac{\epsilon\pi h r^2}{2}\right)} = \frac{\int_{\Delta V}\left(J_1\left(\frac{2.405\rho}{r}\right)\right)^2 \mathrm{d}v}{0.269475\left(2\pi h r^2\right)} \qquad (2.64)$$

where 0.269475 comes from the integral of the Bessel function.

If the volume of the defect is sufficiently small compared to the volume of the cavity, Bessel function can be considered as constant. On the other hand, when a realistic volume integral is taken by applying appropriate boundary conditions, sensitivity increases (Nelatury and Nelatury, 2014).

CHAPTER 3

CAVITY DESIGNS AND SIMULATIONS

There are certain electromagnetic criteria to be considered in the design of an elliptical cavity. First, it is necessary to match the frequency of electromagnetic wave generated by the power supply to the desired mode of the cavity. The length of direction in which particles will move within the cavity should then be designed in accordance with the frequency and velocity of particle bunch. In addition, the normalized PSEF and PSMFD should be minimized, while the quality factor, e.g. the geometry factor, and the R_{sh}/Q values should be maximized. Furthermore, CTCC and field flatness should be kept as high as possible.

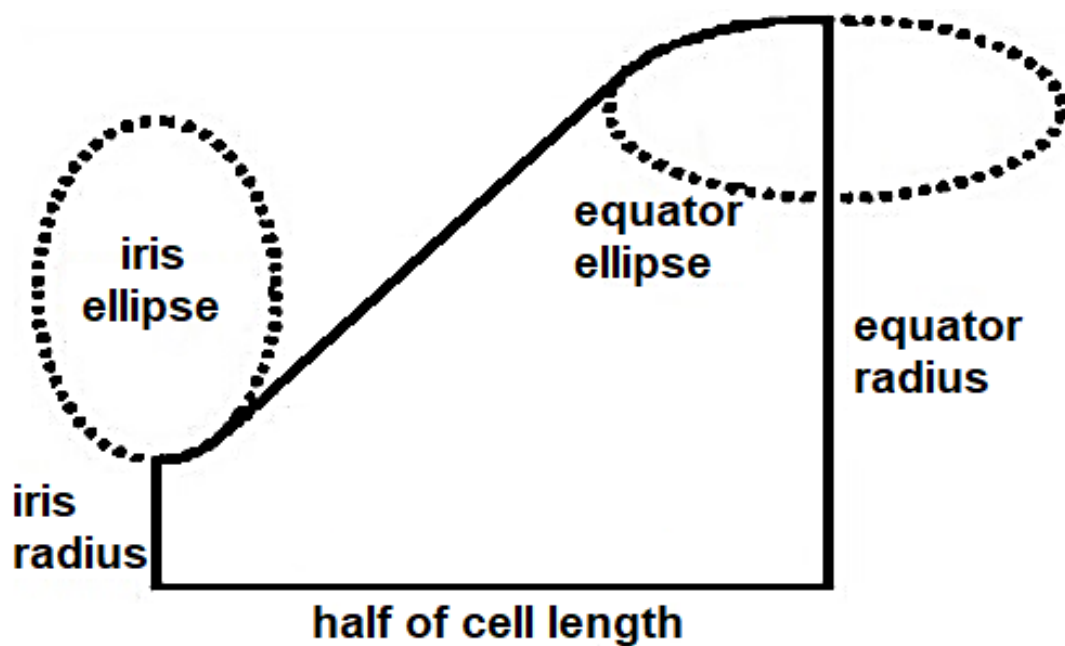Figure 3.1. Geometric Parameters of an Elliptical Cavity

The "cell length" parameter in Figure 3.1, is directly related to transit time of the particle bunch; hence the velocity of the particles. The bunch velocity, frequency of the RF signal and length of the structure should be optimized altogether according to the design demands. Accordingly, the formulation of cell length is given as follows.

$$L_{cell} = \beta\lambda/2 \qquad\qquad (3.1)$$

where L_{cell} represents the cell length, β is the particle speed normalized to speed of light and λ stands for the wavelength of electromagnetic field inside the cavity.

Moreover, equator radius and iris radius are the parameters that can vary the resonant frequency of the cavity (Pagani et al., 2001). Iris radius also provides optimization of the CTCC (Wang et al., 2005). In addition, equator ellipse and iris ellipse sizes change the normalized PSMFD and normalized PSEF values, respectively (Mittal et al., 2011).

3.1. 9-cell 3.9 GHz Elliptical Cavity Simulations

This section is devoted to design a multicell cavity with small CTCC, which is highly affected by geometric variations. Thus, when a tiny cell misalignment occurs, its impact on the electric field can be clearly seen on simulation because N^2/k_{cc} is directly related to sensitivity. At the same time, the other fundamental parameters of the cavity have optimum values. Moreover, the negative consequences of misalignment in this cavity are examined.

The geometric parameters in Figure 3.1 must be chosen correctly in order to optimize these fundamental parameters. The equator radius must be selected at the beginning for frequency adjustment and other parameters must be set on it. Since the beta value of the bunch is considered to be approximately 1, the half of cell length should be equal to one fourth of the wavelength. Also, for the iris radius determination, it is necessary to choose one of the CTCC and R_{sh}/Q values. Larger iris radius increases CTCC so the sensitivity of fields inside the cavity due to geometric changes decreases. On the other hand, the smaller iris radius increases the R_{sh}/Q value and acceleration efficiency. Since the purpose of designing this cavity is to observe the effects of cell alignment errors on electromagnetic fields, both the acceleration efficiency can be increased and the effects of geometric variations can be observed more easily by selecting a small iris radius.

As with all FEM solvers, the issue of determining the number of mesh required in this program is challenging. It was observed that the results converge after 4.5 million tetrahedral meshes by the method of increasing the number of meshes gradually and comparing the results with the previous mesh number. The same method was applied for all other types of solver and cavity.

3.1.1. Cavity Design

The view of inside of the cavity in the simulation program and its geometric parameters can be seen in Figure 3.2 and Table 3.1, respectively.
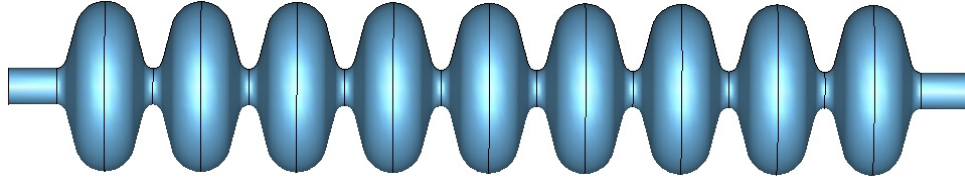

Figure 3.2. 9-cell 3.9 GHz Elliptical Cavity (Source: Karatay and Yaman, 2018)

The cavity is symmetrical in the 3 axes and the lengths of end half-cells are 0.1 mm longer than the other half-cells to optimize field distribution. It should also be noted that the major axis of the iris ellipse is the vertical axis while the major axis of the equator ellipse is the horizontal axis.

Table 3.1. 9-cell 3.9 GHz Elliptical Cavity Dimensions

Geometric Parameter	Value (mm)
Equator Radius	33.91
Iris Radius	7.26
Half of Cell Length	19.17
Major Axis of Equator Ellipse	24.02
Minor Axis of Equator Ellipse	23.96
Major Axis of Iris Ellipse	10.02
Minor Axis of Iris Ellipse	8.02

Due to the small iris radius, CTCC is lower than an average elliptical cavity but field flatness is close to 1 despite small size of the iris. On the other hand, the obtained geometric shunt impedance ($\beta = 1$) was quite high. Some fundamental cavity parameters and field flatness graph which are obtained with this design can be seen in Table 3.2 and Figure 3.3.

Note that, the difference between zero-mode and π-mode is less than 10 MHz, and this situation causes indistinguishable peaks in the F-solver or vector network analyzer screen in experiment even for high-Q normal conductive cavities whose typical

quality factor is $\sim 10^4$. On the other hand, the E-solver provides more accurate analysis opportunity to observe all 9 modes from zero-mode to π-mode of a 9-cell elliptical cavity. Similarly, the electric field plot on the beam axis was obtained in E-solver without being affected by external factors (i.e. excitation source) while the measurement line is located at the center of the cavity from the left beam-pipe to the right one. The acceleration gradient is calculated assuming that the beam-pipes are not included in the cavity length.
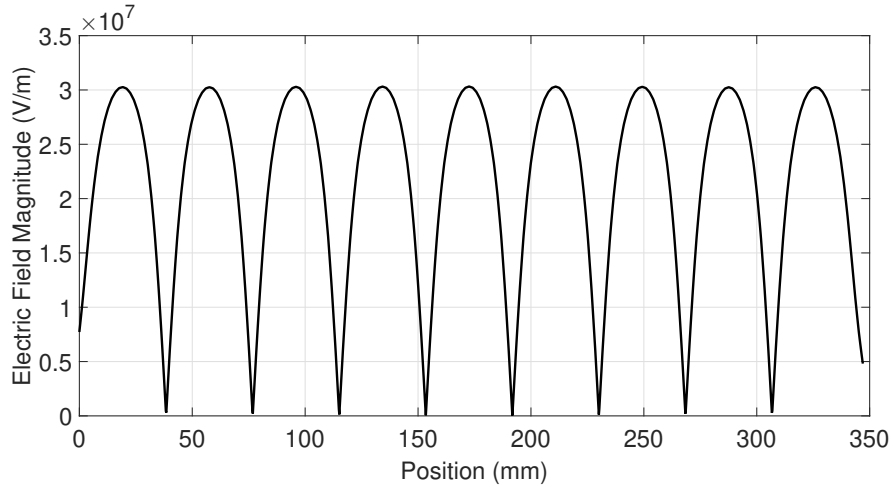

Figure 3.3. Electric Field Magnitude on the Beam Axis

Table 3.2. Fundamental Cavity Parameters of 9-cell 3.9 GHz Cavity

Fundamental Cavity Parameter	Value
Geometric Shunt Impedance (Ω)	1330
Normalized PSEF	1.84
Normalized PSMFD (mT/(MV/m))	4.28
Geometry Factor (Ω)	99.71
Cell-to-cell Coupling	0.19%

3.1.2. Equator Misalignment

As mentioned in Chapter 1, the elliptical cavities are generally produced in the form of half-cells and turned into dumbbells, and then these dumbbells are bonded to-

gether. During this process, alignment errors are likely to occur between the dumbbells. In this section, simulations are performed assuming an alignment error occurs during welding of the dumbbells. The definition of cell misalignment is shown in Figure 3.4, and multi misalignment case is ignored for these simulations. The region where the bunch enter the cavity is called input, and from which the cavity exits is called output, and in the case of misalignment, the beam axis is assumed to be centered at the output. From the first cell to the fifth cell, it is assumed that there is an error in equator welding up to 0.8 mm and individual simulations have been performed for each cell. Note that, the structure is symmetric so the alignment error is simulated until the fifth cell. In other words, since the alignment error in the third cell and the alignment error in the seventh cell give the same result, there is no need to simulate the misalignment between sixth and ninth cells.
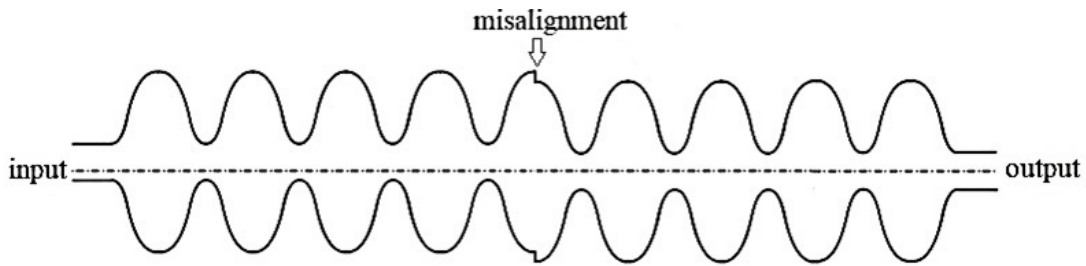

Figure 3.4. Equator Misalignment on the Fifth Cell of a 9-cell Cavity

One of the main problems with the alignment error is the deterioration of field flatness in the cavity. This results in a reduction in acceleration efficiency compared to the aligned form of the cavity. On the other hand, parameters such as normalized PSEF, normalized PSMFD, geometric shunt impedance are directly dependent on the electric field on the beam axis or its line integral. Figure 3.5 illustrates how a 0.8 mm misalignment in the fifth cell affects the electric and magnetic fields inside the cavity. Note that, the peak surface electric and magnetic field values do not occur in the misalignment region, and the simulations to be shown in the following sections are performed under this assumption.

Basically, each cell acts as an RLC circuit, and the alignment error in the equator region causes these RLC values to change. In this case, the field flatness obtained without the alignment error will deteriorate. Capacitive value of the cell with the misalignment increases, thus decreasing the amplitude of the electric field in the misaligned cell. On the other hand, the amplitude of the electric field increases in the cells away from the

33

misaligned cell. This clearly shows us that the acceleration gradient decreases even if the volume integral of the electric field is the same. On the other hand, the deterioration of normalized PSEF and PSMFD values can be understood since the electric field and magnetic field values increase in the cells that are away from the alignment error and at the point where the alignment error occurs.
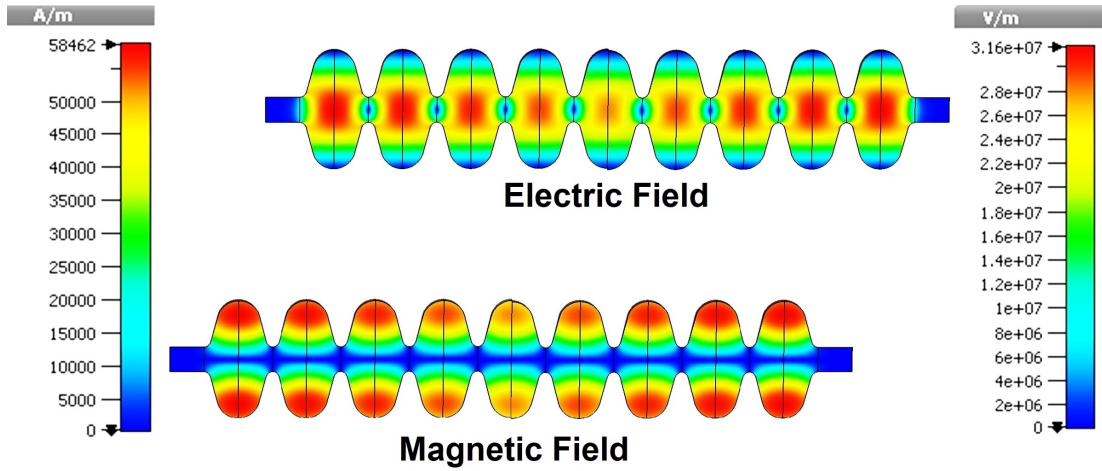

Figure 3.5. Electric and Magnetic Fields with Misalignment (Source: Karatay and Yaman, 2019a).

As seen in Figure 3.6, the simulated 4 cavity parameters deteriorate in case of misalignment. Geometric shunt impedance and geometry factor are the parameters which must be maximized while peak electric and magnetic fields are desired to be as small as possible. All the parameters except for geometry factor are affected more by the cell misalignment on end cell. On the other hand, the cell misalignment on middle cell is the most effective one on the geometry factor parameter.

Remember that due to the misalignment, the beam axis approaches in the iris region in some cells. Under normal conditions, the TM_{010} mode is excited in each cell of the elliptical cavity so there is no transverse component of the electric field at the center. However, in the iris region, the electric field has normal components towards the wall, and if the particles approach the iris wall due to misalignment, they are exposed to transverse kick. As the particles move in the $\vec{z}$ direction, the misalignment occurs in the $\vec{y}$ direction. As shown in the Figure 3.7, the y component of the electric field that is normally converging to 0, appears as 3 peaks in case of misalignment in the third cell. A particle bunch does not move uniformly from the center. Nevertheless, the alignment error increases the number of particles approaching the iris wall and causes particle loss.
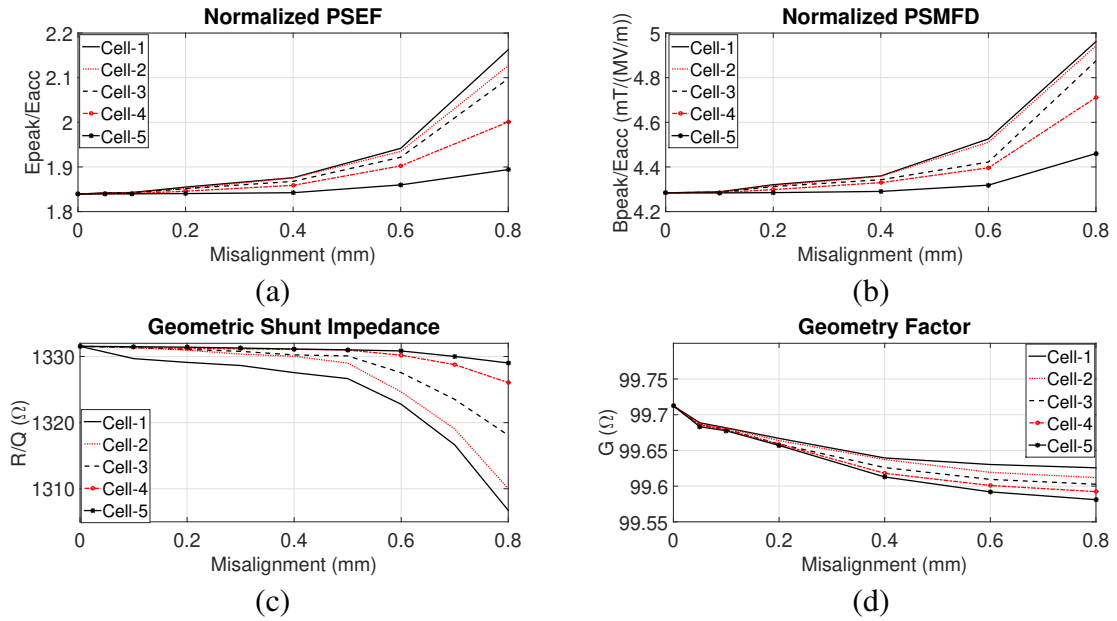
34

Figure 3.6. Effect of Cell Misalignment on the Fundamental Cavity Parameters (a)
Normalized PSEF (b) Normalized PSMFD (c) R/Q (d) G
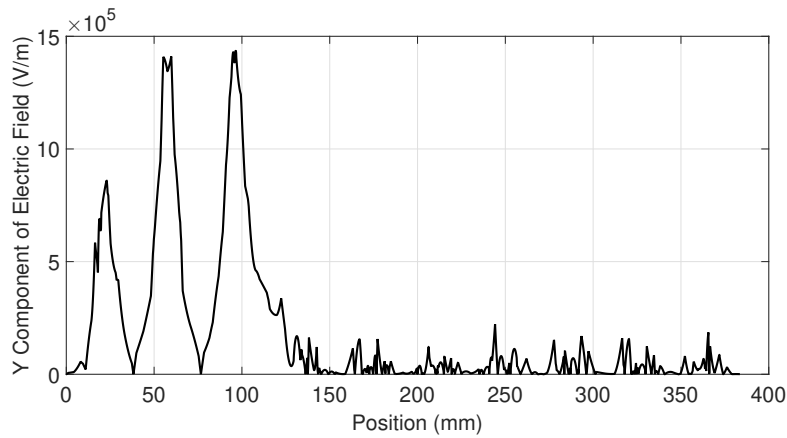

Figure 3.7. Transverse Kick due to Misalignment on Cell 3

3.1.3. Treatment of Equator Misalignment

Each cell of the elliptical cavity can be considered as a parallel RLC circuit, and
the equatorial misalignment error can be modeled as an increase in C and a decrease in L
and R. If we accept the cell alignment error as an inevitable fabrication error, the treatment

of this condition can be performed by the perturbation tuning method by observing the measurement results (Bellantoni et al., 2003). At this point, the primary objective is to restore the electric field peaks on the beam axis of the cavity to correct the frequency shift and to equalize the electric field values held in each cell. In fact, perturbation tuning is a method used to correct the consequences of all possible mechanical errors, not just for cell alignment error. The electric and magnetic field value of the faulty cell can be restored by means of a compressor moving parallel to the beam axis, see Figure 3.8.
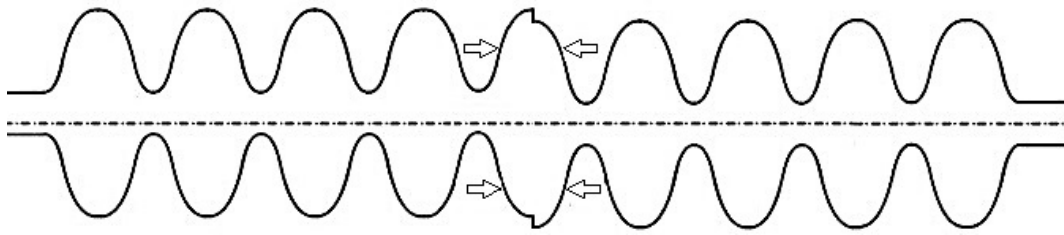

Figure 3.8. Mechanical Tuning

In the CST-MWS software, trial simulations are performed by changing the length of the cell on the acceleration axis of the cell where the alignment error is created and the field flatness approaches to 1 again. If you recall, geometric shunt impedance, normalized PSEF, and normalized PSMFD parameters are related to the acceleration gradient, and these parameters have been restored with the improvement of the acceleration gradient. It is worth to note that the normalized PSEF and PSMFD values of the cavity occur in the iris region and below the equator, respectively. For the alignment error up to 0.8 mm, the peak surface field values do not occur at the point of misalignment. If the misalignment value is increased to cause peak electric and magnetic field to occur in the area of misalignment, these values would not be completely restored by perturbation tuning. In addition, the increase in the electric field in the direction of misalignment, which we call transverse kick, and the decrease of the quality factor, i.e. the geometry factor, cannot be corrected by perturbation tuning, but rather become worse. When the energy inside the cavity is constant, the surface integral of the magnetic field of the misaligned cell rises and Q decreases even further. While the geometry factor of the misaligned cavity before tuning was approximately 99.6 Ω, it decreased to 99.3 Ω after tuning. Similarly, the value of the electric field held by the misaligned cell and the electric field around the iris wall of that cell increase. Therefore, the transverse kick value further increases, especially when we are tuning the alignment error in the first cell, see Figure 3.9.
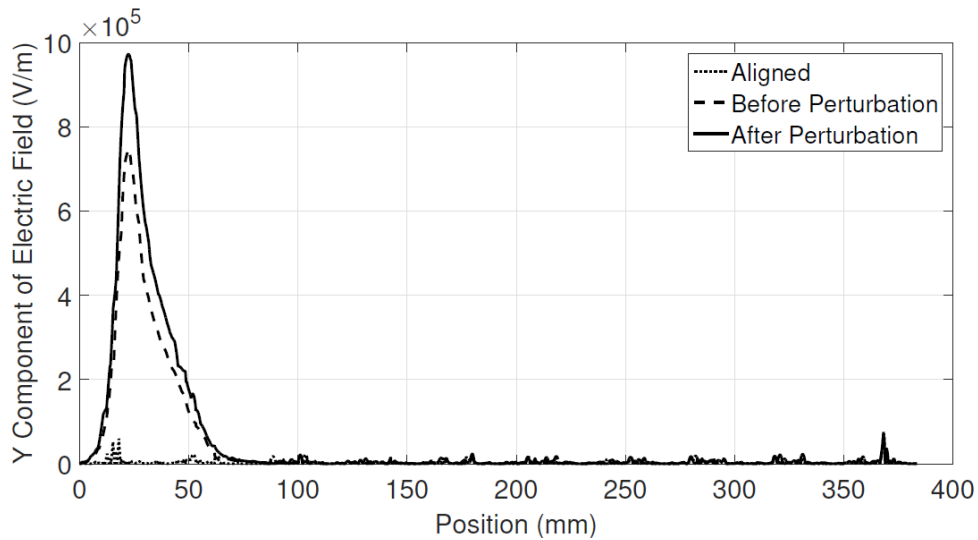
Figure 3.9. Effect of Mechanical Tuning on Transverse Kick

If the equator alignment error occurs in more than one cell, the first consideration is how close the field flatness is to its original state. In this case, field flatness can be theoretically approached to 1 with multiple misalignment, but this is not useful enough due to multiple transverse kick and drop in the quality factor. For instance, the longitudinal electric field distortion of a 0.8 mm alignment error in the first cell can be eliminated by an alignment error of 0.8 mm in the fifth cell and 0.6 mm in the ninth cell of this cavity. However, this means that the particle bunch will be subjected to more transverse kick across all cells and at the same time the power lost to heat will increase.

3.1.4. Wakefield Solver Simulations

The simulations with wakefield solver consist of two main topics. First, the effects of cell alignment errors on wakefield were observed. Subsequently, surface roughness was modeled with Huray's snowball model and its effects on wakefield and impedance were examined. Although Huray's snowball model was originally proposed for microstrip lines, it is useful to express increased surface roughness with increased surface impedance.

This solver allows us to define the length, velocity and shape of the particle bunch on the beam axis. By default, a Gaussian bunch can be defined, but a particle bunch can be generated in a way that can be imported from an external source. On the other hand, it is possible to define which beam pipe the particle beam will center in a misaligned cavity.

The axis of motion of the particles and a cross-section of the cavity can be seen in Figure 3.10.
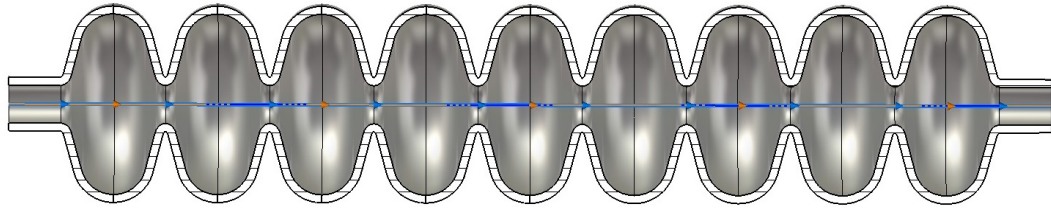

Figure 3.10. Elliptical Cavity and Particle Beam in Wakefield Solver

3.1.4.1. Effect of Surface Impedance on Wake Field

A simple rectangular test cavity with 5.8×10^7 S/m conductivity was first designed to investigate the applicability of a model designed for microstrip lines to the cavities. The TE_{101} mode of this cavity was then excited using the frequency domain solver of the CST. Then, simulations were performed using 2 different approaches. Firstly, a total of 240 defects whose amplitudes are 0.1 mm were placed on the surface of the cavity and the results on the electric field and losses were examined. Then, with Huray's snowball model, the conductivity value of the smooth surface cavity was expressed as a complex number and simulated again. At this point it is important to determine the appropriate coefficients of Huray's model and these coefficients were determined with trial and error. The impedance coefficients of the frequency components were changed until the metal losses were equalized and the result in Table 3.3 was obtained while the input power is 500 mW. On the other hand, when an electric field measurement axis is drawn parallel to the long edge, centering the surface perpendicular to the longest edge of the cavity, the electric field profile in Figure 3.11 is obtained.

Note that, real roughness refers to the actually added 240 Gaussian defects on the surface of the cavity, while virtual roughness means that the boundary conditions of the cavity are defined as complex surface impedance. Both approaches in terms of metal losses and changes in the electric field are in agreement. However, the simulation time is more than 12 hours in the number of meshes converge by real roughness, while the simulation time in surface impedance approach is 18 minutes. Since there is such a

difference even in a simple structure such as a rectangular cavity, the surface impedance approach seems inevitable for a complex structure such as an elliptical cavity.

Table 3.3. Comparison of Defects in terms of Metal Loss

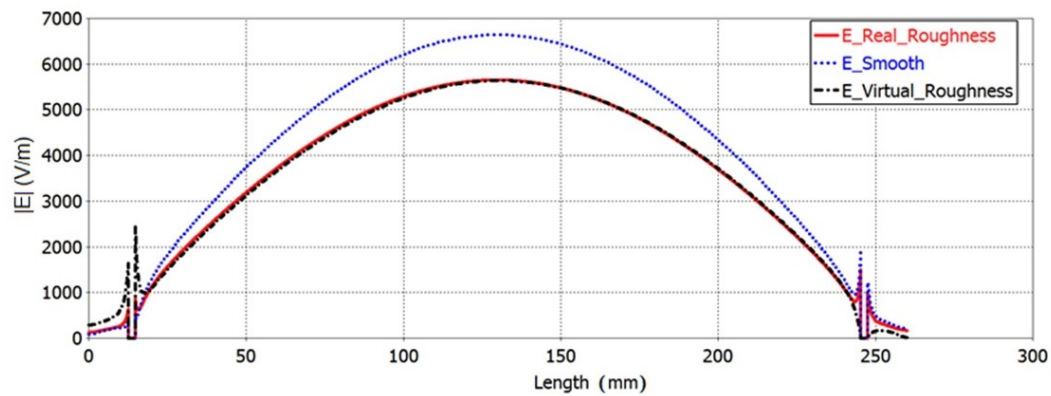| Case	Loss (mW)
No defect	59
Real Defect	66
Empirical Surface Impedance	66

Figure 3.11. Electric Field of TE_{101} Mode of a Rectangular Cavity (Source: Karatay and Yaman, 2019a)

After the confirmation of Huray's snowball model application for the rectangular cavity, the relationship between the surface impedance of the cavities and the remaining electromagnetic fields left behind by a particle passing through an elliptical cavity can be examined. The walls of the elliptical cavity were formed of copper with a bulk conductivity of 5.8×10^7 S/m with smooth surface and having surface impedance of $0.53 + j*0.53$ Ω, respectively. Subsequently, a 10 mm long positively charged particle bunch having Gaussian shape in longitudinal axis with 10 nC total charge was injected into the cavity. As shown in Figure 3.12, the increased surface impedance allows wake field to dampen at a closer distance.

In the frequency domain, see Figure 3.13, compatible results naturally can be seen such that higher the surface impedance, lower the wake impedance value. The monopole mode wake impedance for the smooth cavity is 0.27 MΩ, while wake impedance of the

other cavity for the same mode is 0.17 MΩ. In the first higher mode, the wake impedance value is 0.16 MΩ in the smooth cavity and in the other one 0.08 MΩ.
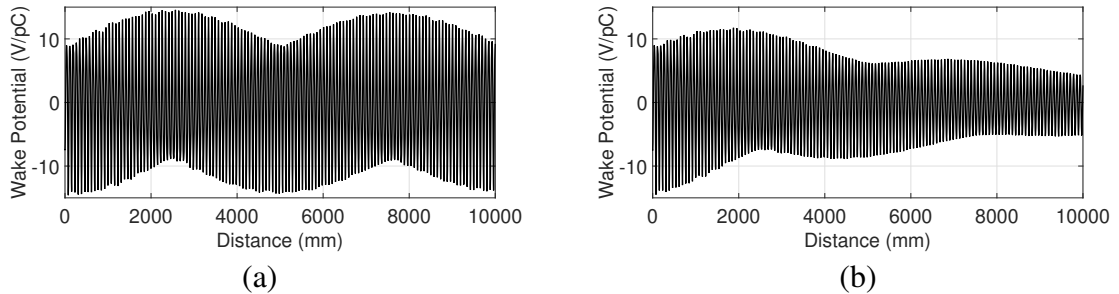

Figure 3.12. Longitudinal Wake Potential (a) Original Cavity (b) Defected Cavity
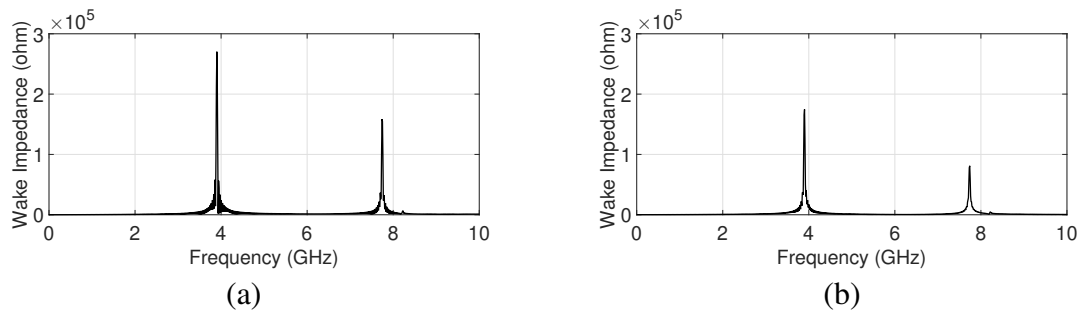
Figure 3.13. Longitudinal Wake Impedance (a) Original Cavity (b) Defected Cavity

3.1.4.2. Effect of Equator Misalignment on Wake Impedance

Assume that the particle's trajectory is along the $+\hat{x}$ direction, and an alignment error occurs in the $+\hat{y}$ direction. The most important point to note here is that, unlike the E-solver, there is no longer a symmetry on the longitudinal axis. That is, the error in the first cell and the error in the last cell cause different electromagnetic effects. Suppose the particle bunch is centered on the beam-pipe contacting the first cell. In the case of the alignment error of the first cell, the particle bunch will pass through the 9 misaligned cells. On the other hand, in the case of the alignment error in the ninth cell, the number

of misaligned cells through which the particle bunch passes is only 1. In this case, it is expected that the transverse wake impedance will be greater, which will be caused by the alignment error in the first cell, see Figure 3.14. For the alignment error in the first cell, the transverse wake impedance of the first higher order mode rises to $\sim$10 kΩ. Additionally, it is approximately 4 kΩ for the alignment error in the fifth cell, and several hundred ohms for the alignment error in the ninth cell. One can notice that transverse wake impedance of higher order modes are more affected by monopole modes due to equator misalignment. On the other hand, longitudinal wake impedance of neither the monopole modes nor the higher order modes are significantly affected by cell alignment error.
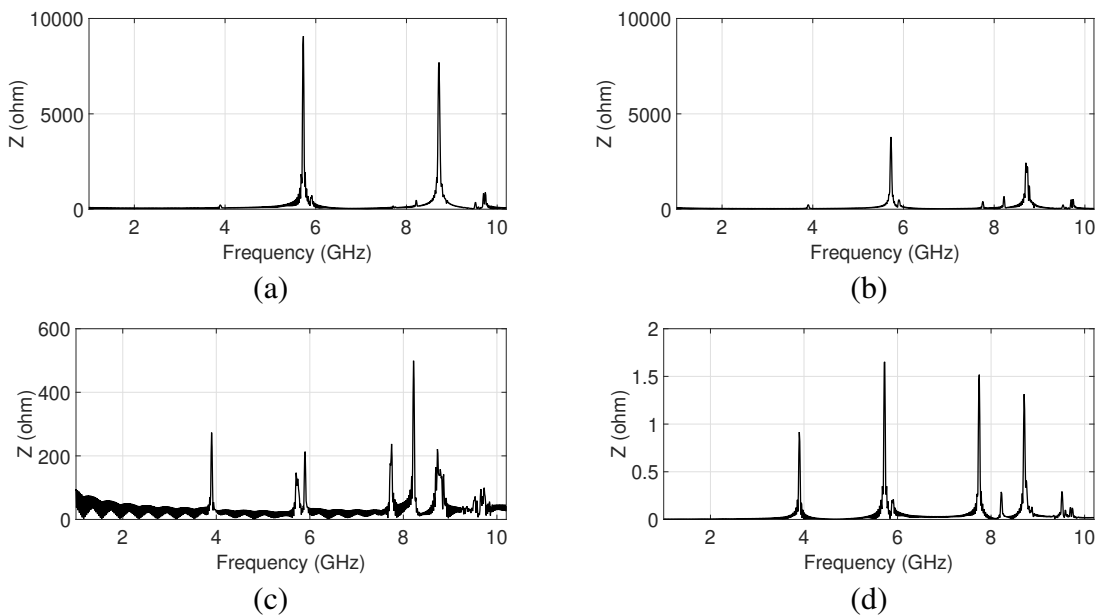
Figure 3.14. Effect of Misalignment on Transverse Wake Impedance (a) Misalignment on Cell 1 (b) Misalignment on Cell 5 (c) Misalignment on Cell 9 (d) No Misalignment

3.1.5. Iris Misalignment

Simulations were performed not only for the equatorial misalignment but also for the misalignment in the iris region. In this context, the same simulations of equator misalignment were performed for the iris misalignment and the same parameters were observed. The results for aligned case and 0.8 mm misalignment are listed below. Alignment

errors in the first cell and the fifth cell were individually simulated in order to compare the significance between the middle cell and the end cells. It should be noted that in the iris alignment error, the error on the first cell means that the first cell is on an axis 0.8 mm different from the other eight cells. On the other hand, if we call the error on the fifth cell, it indicates that the first five cells are located on a different axis than the other four cells. According to Table 3.4, just like the equator misalignment, the end cell is more important for the geometric shunt impedance and normalized PSEF and PSMFD parameters, while the geometry factor is more affected by the misalignment in the mid cell.

Table 3.4. Effect of Iris Misalignment on Fundamental Cavity Parameters

Parameter	Aligned	0.8 mm on end cell	0.8 mm on mid cell
R/Q (Ω)	1334	1294	1329
Normalized PSMFD (mT/(MV/m))	4.3	5.1	4.6
Normalized PSEF (unitless)	1.84	2.20	1.99
G (Ω)	99.72	99.65	99.57

3.2. 2 GHz and 3.9 GHz 3-cell Elliptical Cavity Simulations
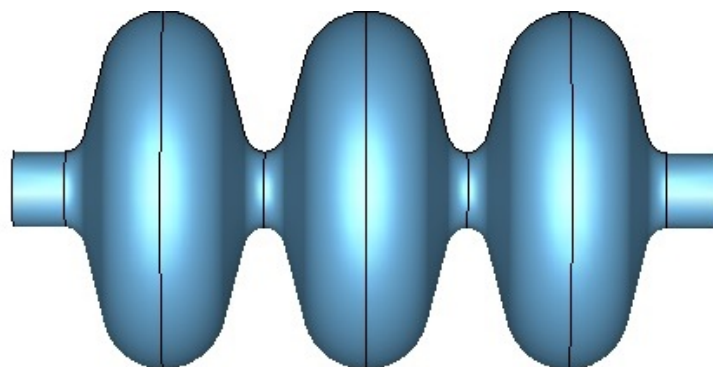

Figure 3.15. 3-cell 2 GHz Elliptical Cavity

After 9-cell 3.9 GHz elliptical cavity simulations, the first question that comes to mind is whether our findings are only valid for this structure or not. Therefore, it is

necessary to examine if this behavior depends on frequency and cell number. For this purpose, the same structure whose π-mode is at 3.9 GHz was scaled to 2 GHz and the number of cells is reduced from 9 to 3, see Figure 3.15. For the field flatness optimization, small changes have been made to the end half-cells and more than 99% field flatness has been achieved. In addition, this new structure is scaled to 3.9 GHz and has been subjected to the same simulations. It is known that, the normalized PSEF and PSMFD values are related to the acceleration gradient, and the electric field value in the misaligned cell decreases. Therefore, simulations were performed for the geometric shunt impedance and geometry factor values. In addition, new simulation was performed to determine the frequency shift, see Figure 3.16. Even at a very exaggerated level of misalignment, the frequency shift is in the order of a few kilohertz. The frequency shift at this level can be treated by a tuning method, easily. Therefore, the frequency shift is not the main problem in this case. It should be noted that, since the frequencies are different, the misalignment value is expressed as the electrical length for a consistent plot.
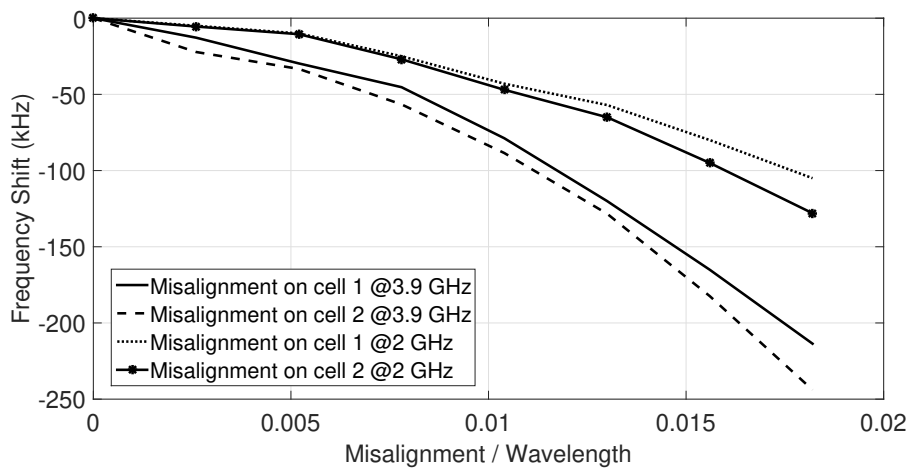
Figure 3.16. Frequency Shift of 3-cell 2 GHz and 3.9 GHz Elliptical Cavities

As can be seen in Figure 3.17-3.18, just as in the 9-cell cavity, while the middle cell has more effect on the geometry factor than the end cell, the end cell is more effective than middle cell for R_{sh}/Q value. The decrease in the geometry factor may not seem too high, but it should be noted that this value essentially indicates a decrease in the quality factor. In a cavity with very high quality factors, even a deterioration in this level can cause a very high power to be converted to heat. Note that, since the G values of each 2 cavities in the aligned case are different, the y-axis is normalized to 1.

The results of the 9-cell 3.9 GHz cavity and the 3-cell cavities regarding which cell is more effective on which parameter are highly consistent. It is important to clarify that this behavior is valid for different number of cells and frequencies.

Figure 3.17. R_{sh}/Q Change of 3-cell 2 GHz and 3.9 GHz Elliptical Cavities
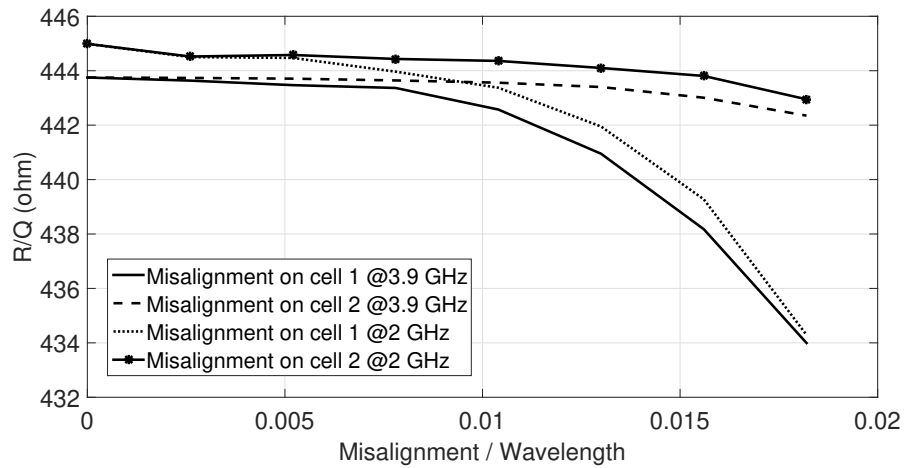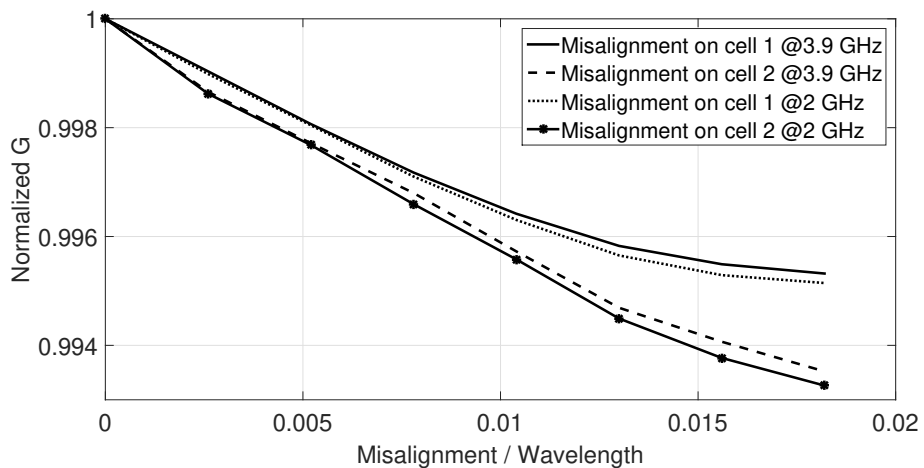

Figure 3.18. G Change of 3-cell 2 GHz and 3.9 GHz Elliptical Cavities

CHAPTER 4

FABRICATIONS AND EXPERIMENTAL RESULTS

Two different elliptical cavities were simulated and fabricated in order to observe the information obtained from the simulations and experiments. One of these cavities is a 3-cell, high CTCC cavity operating at 3.9 GHz and has been fabricated using 3D printing technology. The second cavity is a single cell cavity operating at 2.45 GHz, and this cavity is carved from a metal block by CNC machine.

4.1. 3-cell 3.9 GHz Elliptical Cavity

Cell-to-cell coupling is a value proportional to the difference between zero-mode and π-mode and increases with expanding iris radius (Sulimov et al., 2016). If the quality factor of the cavity to be fabricated is not high enough and the CTCC is low, the peaks to be observed in the weak coupling measurement begin to interfere each other. Therefore, in order to increase the CTCC, the iris radius was raised too high and the frequency difference between the monopole modes increased such that iris diameter is 5 cm while the equator is 7 cm. On the other hand, it is known that there is a relationship between the cell number, CTCC and sensitivity (Li and Adolphsen, 2008; Sekutowicz et al., 2003).

$$Sensitivity \propto \frac{N^2}{k_{cc}} \tag{4.1}$$

Note that, it would be very difficult to observe the deterioration of the field profile. Hence, the level of misalignment has been increased to exaggerated values, like 4.6 mm and 9.2 mm.

4.1.1. 3D Printing and Conductive Coating

Using white PLA and ABS filaments with a 3D printer, a 3-cell elliptical cavity whose π-mode is at 3.9 GHz was fabricated. The structure consists of 4 parts, 2 end

cells including beam-pipes and 2 dumbbells. There are 3 screw holes on the 4 corners of each part and the parts are connected to each other with these screw holes. Each hole is adjusted to M4 screws whose diameter is 4 mm, but the diameter is chosen as 4.1 mm, leaving 0.1 mm of fabrication tolerance. The center of each screw hole is 4.6 mm apart, and the distance between these holes gives us an opportunity to create misalignment. This provides a possibility of creating 3 levels of misalignment in the equatorial region of each cell, see Figure 4.1.

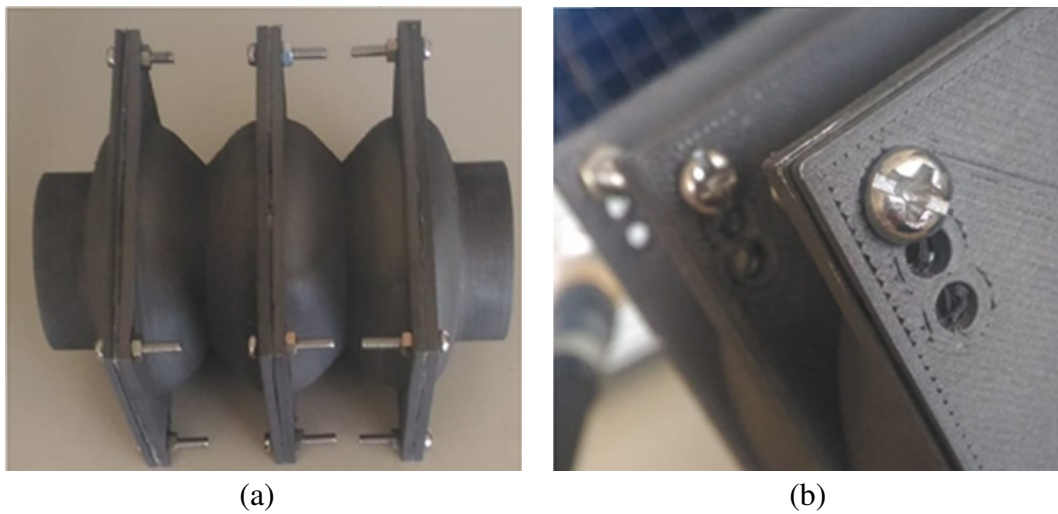| (a) | (b) |

Figure 4.1. Nickel Coated Cavity (a) Screwed Cavity (b) Screw Holes (Source: Karatay and Yaman, 2019a)

The initial structure was a bit rough due to the failure of the 3D printer, but it has been reduced with a fine sandpaper. After that, nickel coating spray was used to make the cavity fabricated from insulating materials conductive. There have been numerous studies that make a non-conductive object conductive and use it as a microwave device. In addition to nickel plating, copper plating (Kyovtorov et al., 2017; Tak et al., 2017) and silver plating (Bal et al., 2019) are also preferred. In this work, nickel particles are placed in some kind of aerosol and there is a bead inside the bottle. This bead ensures homogeneity in the bottle if it is shaken continuously for 2 minutes before use. After shaking sufficiently, the target must be sprayed from 25-50 cm distance, preferably 30 cm. If the nickel is sprayed from far away, adequate coating may not be achieved. If it is sprayed too closely, the shape of the structure may not be preserved. After coating, it must be allowed to dry for 6-10 minutes and must not touch the coated object during this time. It takes 24 hours at room temperature to dry completely. It can be plated more than once

to reduce surface resistance thoroughly, but does not cause significant changes after the third coating (MG-Chemicals, 2013). If the temperature is increased, the drying time can be shortened, but since the ABS and PLA filaments can easily melt in hot environments, drying was carried out at room temperature.
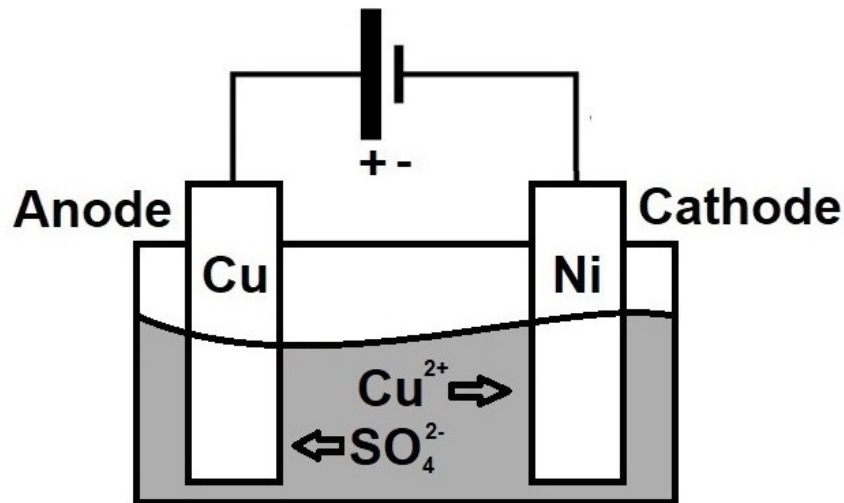

Figure 4.2. Electroplating System (Source: Karatay and Yaman, 2019b)

Although the CTCC of the cavity increases, the conductivity has to be further increased because the surface of the cavity is still rough and the conductivity of the nickel coating was too far from the bulk nickel conductivity. For this reason, electroplating, a coating method that could be applied to a conductive structure, was applied. Water was poured into a glass container with a water-soluble crystal called copper sulphate. The amount of water can be determined by the level at which the structure to be coated will completely enter the water. Copper sulphate should be added until the solution is saturated. Unless enough copper sulphate is added, an appropriate coating may not be made because the ionic conductivity of the solution will be low (Stern et al., 2011). Approximately 250 grams of copper sulphate was added to 1.2 liters of water to form an electrolyte, and it was mixed until the insoluble residues remained at the bottom of the water. A copper plate attached to anode and a nickel coated cavity attached to cathode were placed into the electrolyte. The distance between the anode and cathode was determined to be approximately 15 centimeters by trial and error. Furthermore, the given current value was fixed to about 2 amperes and the voltage value between 3-8 volts has been determined to obtain this. Plating was performed for 1 hour for each side of the cavity parts and each process was carried out with a different solution and a different anode

electrode. Each surface can be electroplated more than once (twice in this work) to ensure adequate copper thickness. An illustration of the copper plating process can be seen in Figure 4.2.

As can be seen in Equation 4.2, at the cathode, copper ions are reduced and converted to solid metal while electrons are flowing to nickel due to potential difference. In this way, the surface of nickel can be coated with copper.

$$\text{Cathode Reaction:} \quad Cu^{2+}_{(aq)} + 2e^- \longrightarrow Cu_{(s)} \tag{4.2}$$
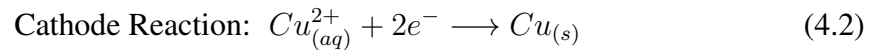
where $Cu^{2+}_{(aq)}$ denotes the copper ions dissolved in the water and $Cu_{(s)}$ indicates the solid copper. Nickel plated and copper plated cavity parts can be seen in Figure 4.3.

(a)   (b)
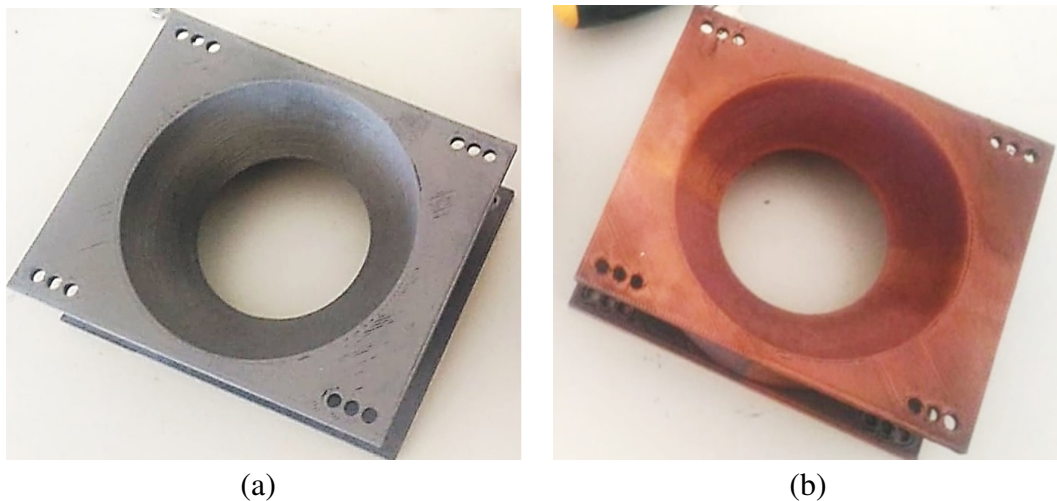
Figure 4.3. Metallization of Cavity Parts (a) Nickel (b) Copper

4.1.2. Experimental Results

Three different measurements were taken for this cavity. First, the quality factors were measured for each level of misalignment with a weak coupling while the cavity was nickel plated, and geometry factors were obtained. The cavity was then plated with copper and quality factor measurements were taken with critical coupling in this state. Finally, to

determine the electric field distribution of the cavity, individual bead-pull measurements were completed for 4.6 mm of misalignment on each cell.

4.1.2.1. Measurements of Nickel Coated Cavity

Before the cavity is coated with copper but still conductive, quality factor measurement was taken. Measurement and simulation results can be seen on the same graph, see Figure 4.4. Note that, this measurement was taken when there was no misalignment in the cavity.

In order to measure the quality factor of the cavity with weak coupling, it is necessary to first calibrate VNA with 2-port calibration. The S_{21} value is then monitored by an antenna to be inserted through the beam-pipe regions of the cavity. The most important consideration during this process is that the antennas are coupled to the cavity very little. This reduces the effect of the external circuit. If this process was done with a high coupling, the coupling quantity should be determined, and measured value must be multiplied by $(1 + CF)$ to determine unloaded quality factor. In this case, however, since the coupling value is very close to zero (see S_{21} values), the measured value is almost equal to the unloaded quality factor.

Three peaks appear in the figure, the first peak corresponds to zero-mode and the third one denotes the π-mode. Especially in π-mode, simulation and measurement give approximately the same results. There are some differences in the frequencies of the other 2 modes. When coating the cavity, changes in cavity volume and iris radius may have changed the CTCC and frequencies of some modes.

It is worth to note that the conductivity in the simulation value was adjusted based on the measurement result. The quality factor of the π-mode obtained in both simulation and measurement is ~ 105. To find the geometry factor of the cavity, the measured Q value should be multiplied by the surface resistance. The effective conductivity value of about 1800 S/m gives us a surface resistance of 2.88 Ω at 3.9 GHz. In this way, when the geometry factor is calculated, 303 Ω for the aligned case is found.

The geometry factor values obtained for the misalignment of 4.6 mm and 9.2 mm for the first and second cells are in Table 4.1. One can say that these measurement results and the simulation results in the previous chapter agree well. First, the higher the misalignment, the lower the geometry factor value. On the other hand, for the same level of misalignment, the middle cell causes more decrease than the end cell.

Frequency shifts were also examined for each cell alignment error value. How-

ever, it has been observed that the frequency shift is low (less than 1 MHz), even for an exaggerated alignment error that is about 9 mm. In each measurement, it was not possible to draw a meaningful figure for such small frequency shifts, as the amount of insertion of the antenna necessarily changed.
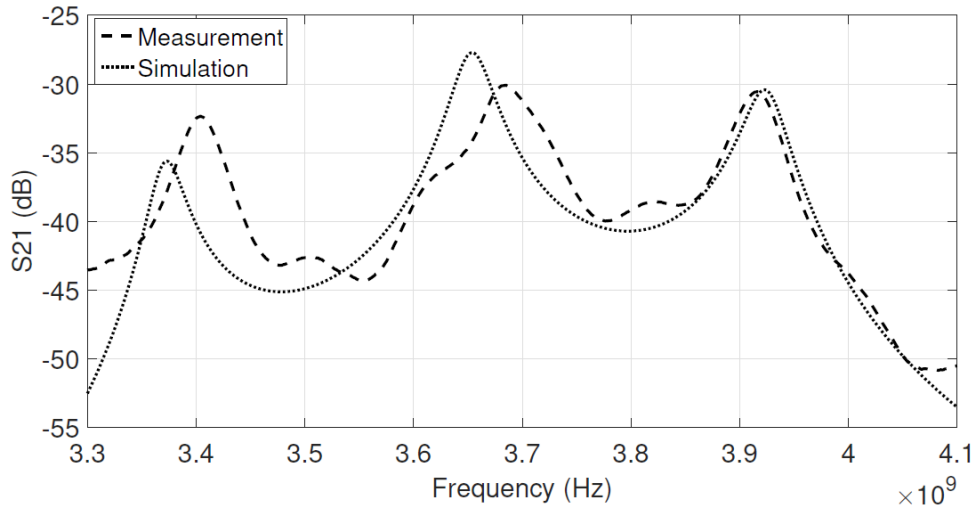
Figure 4.4. S_{21} Results of Monopole Modes of Nickel Coated Cavity

Table 4.1. Geometry Factor of Nickel Coated Cavity

Case	Geometry Factor (Ω)
No Misalignment	302.7
4.6 mm on 1st Cell	270.2
9.2 mm on 1st Cell	204.8
4.6 mm on 2nd Cell	248.8
9.2 mm on 2nd Cell	180.9

4.1.2.2. Measurements for Copper Coated Cavity

An increase in the quality factor is expected after the nickel coated cavity is plated with copper by electrolysis. To determine the difference, the quality factor was measured by critical coupling, not by weak coupling this time. In order to enable the coupler to

be coupled to the cavity at the desired level, covers were attached to the beam-pipes of the cavity and the coupler was fixed to these covers. Because the antenna perturbs the cavity in the electric field region, the resonant frequency of the 3 modes of the cavity has decreased slightly.

The main step that must be done to bring the desired mode into the critical coupling state is to adjust the impedance at the desired resonant frequency closer to 50 Ω. This can be achieved by changing the size and shape of the antenna. Unlike weak coupling measurement, it is sufficient to take measurements from only one-port, thus performing one-port calibration. Since the coupler is critically coupled to the cavity, the effect of the external circuit is observed and to eliminate this effect, measured quantity is multiplied by $(1 + CF)$ to find the actual Q value of the cavity. When the impedance is exactly 50 Ω, it is sufficient to multiply the measured value by 2 since the coupling factor will be equal to 1.
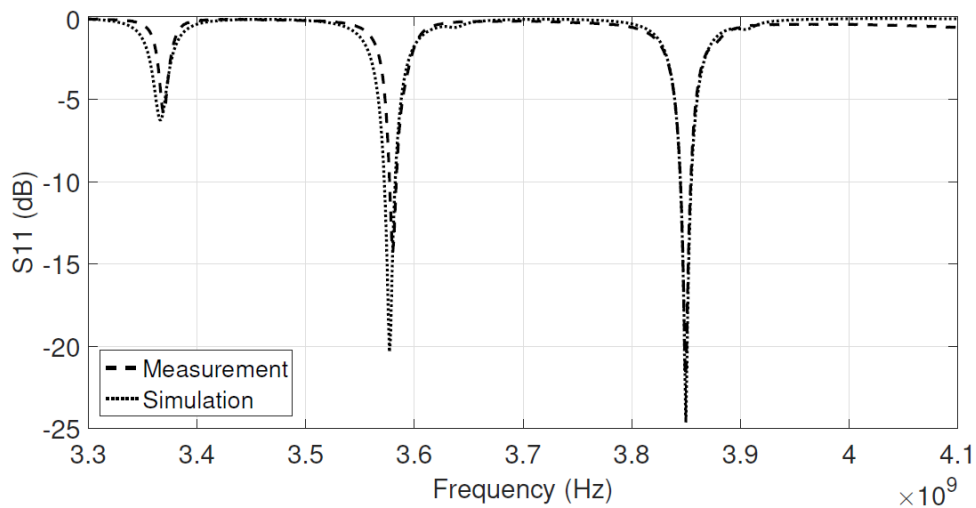
Figure 4.5. S_{11} Results of Monopole Modes of Copper Coated Cavity

Another issue related to the critical coupling measurement is that the impedance generally cannot be exactly 50 Ω, but it can be obtained close enough. Therefore, the value of S_{11} is not equal to zero, but below -20 dB is considered sufficient in our measurements. In this case, whether the cavity is over coupled or under coupled cannot be determined only by looking at the S_{11} plot. For instance, the coupling factor for the S_{11} value of -20 dB can be about 0.82 or 1.22. In this case, one has to check the Smith Chart display and see whether the diameter of the resonance circle is greater than the radius of the Smith Chart or not. If it is greater, the cavity has been over coupled and vice versa (Caspers,

2012; Wang et al., 2017). This approach cannot be used to measure the quality factor with one-port measurement if CF is too close to zero or much larger than one.

Both measurement and simulation results can be seen in Figure 4.5. As with the weak coupling measurement, the measurement here was taken when there was no misalignment.

Geometry factor measurements were performed for end and middle cells belonging to 2 different misalignment levels. It is important to note that the geometry factor is a material-independent parameter and that the cavity is coated with nickel or copper does not change this value. However, during the plating with copper, slight changes in the roughness and shape of the cavity may have occurred. In Figure 4.5, the effective conductivity in the simulation is chosen as approximately 9000 S/m while the curves are almost on top of each other. Hence, the geometry factor value was calculated by using this value. As can be seen in Table 4.2, the most effective cell in the decline of the quality factor is the mid cell, and the higher the level of misalignment, the lower the quality factor. In addition, the values in Table 4.2 are very close to the values in Table 4.1. Note that the measured unloaded quality factor was approximately 240 and the surface resistance was found to be 1.3 Ω. The effective conductivity of the nickel plated cavity enhanced with copper plating and the quality factor increased to more than 2 times.

Table 4.2. Geometry Factor of Copper Coated Cavity

Case	Geometry Factor (Ω)
No Misalignment	314.5
4.6 mm on 1st Cell	281.9
9.2 mm on 1st Cell	216.0
4.6 mm on 2nd Cell	252.4
9.2 mm on 2nd Cell	191.9

Figure 4.6 shows the experimental setup for reflection measurement and 3 deeps on VNA screen. The reflection coefficient value of the third mode displayed on the screen is -22 dB. In this case, it is necessary to determine whether the system is over coupled or under coupled for a precise measurement. For this, when looking at the Smith Chart, 3 circles should be seen in this span. The third one of the three circles numbered in Figure 4.7 corresponds to the third deep in Figure 4.2. Since the diameter of the circle is slightly smaller than the radius of the Smith Chart, the system is actually under coupled. Therefore, the unloaded quality factor can be found multiplying the measured quality
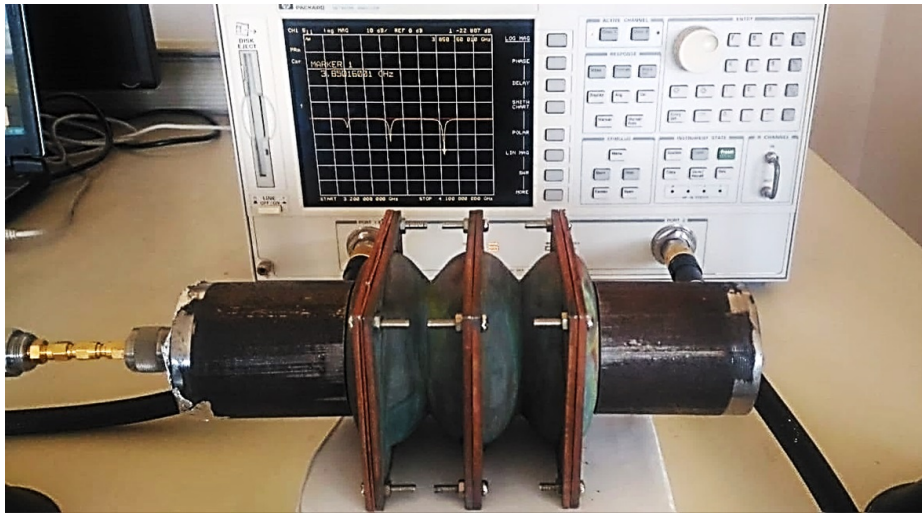
factor by 1.83, not by 2.

Figure 4.6. Reflection Measurement Setup of the Copper Coated Cavity (Source: Karatay and Yaman, 2019a)
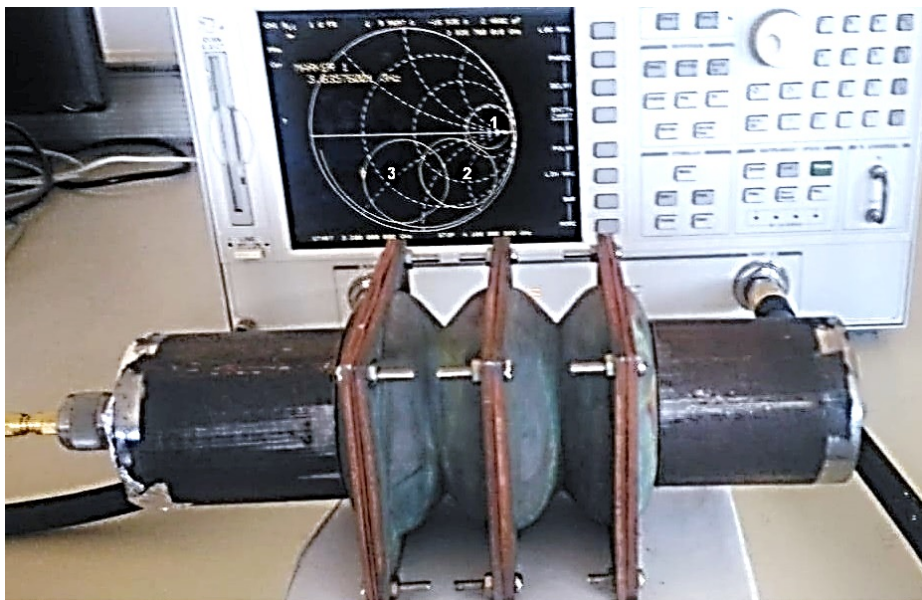

Figure 4.7. Smith Chart of Reflection Measurement

4.1.2.3. Bead-Pull Measurement

Bead-pull measurement is a method used to determine the fields of a cavity with unknown field profile. It is based on the method of pulling a metallic or dielectric bead of sufficiently small dimensions through the cavity. Changes in the behavior of the cavity that is connected to the VNA during this process provide information about the field inside the cavity.

In this study, a metallic bead with a radius of 6 mm was used. Basically, the change in the boundary conditions of the region under investigation causes a change in the resonant frequency of the cavity's corresponding mode. As inferred in Equation 2.63, the frequency decreases if the metallic bead moves from the region where the electric field is dense and the magnetic field values are approximately zero.

An illustration of the bead-pull measurement setup can be seen in Figure 4.8. When the motor, which is driven by a controller, pulls the bead, the cavity is measured by VNA and the data is transferred to the personal computer. The position where the frequency is the lowest is the position with the highest electric field under the assumption that the magnetic field vanishes.
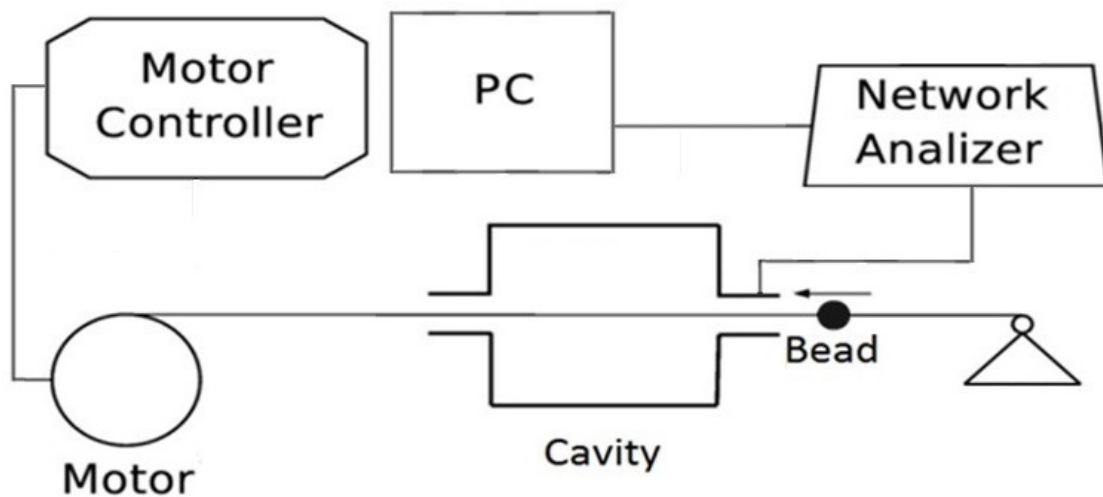

Figure 4.8. An Illustration of Bead-Pull Measurement

The peak frequency shifts obtained in this process was first normalized. Then the square root of the frequency shift was calculated while the electric field amplitude is proportional to that value. The first measurement was performed in the absence of

misalignment in the cavity and was plotted with the normalized form of the simulation result of the E-solver, see Figure 4.9. The peak electric field value in the middle cell is lower than the end cells, and the field flatness is $\sim 95\%$ according to measurements which was obtained $\sim 99\%$ via simulations. The deterioration of field flatness in measurement could be related such as the fabrication accuracy of the 3D printer, surface roughness, changes on the dimensions of the cavity due to conductive coating.
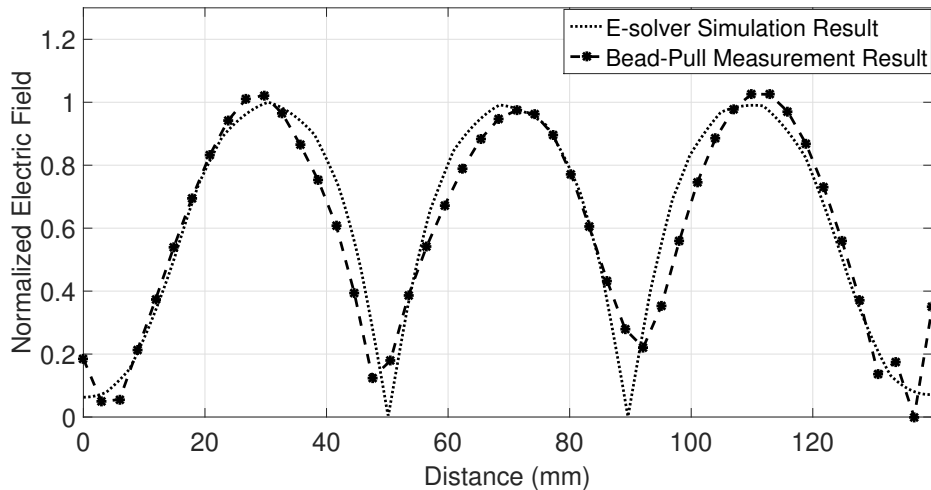
Figure 4.9. Bead-Pull Results of Aligned Case

Afterwards, bead pull measurements were realized by arranging individual misalignments for the first and the second cells. The results of these measurements are illustrated in Figure 4.10-4.11. For the alignment error on the first cell, 90% field flatness is reached according to the simulation results, while the measurement results indicate the field flatness value as 87.7%. On the other hand, in case of misalignment in the second cell, field flatness is 95% according to simulation results, and 88.5% according to measurement results. Since the electric field in the second cell was initially lower than the others, the difference between the simulation and the measurement results enhances in this figure. However, it can be seen that the magnitude of the electric field in cell with the alignment error is reduced and this deterioration causes electric field rises for the end cells. The simulation and the measurement results agree on the field flatness deteriorates further in the case of misalignment in the first cell. This effect can be seen more clearly via simulations since it is originally assumed that field flatness to be 100% while there is no misalignment.
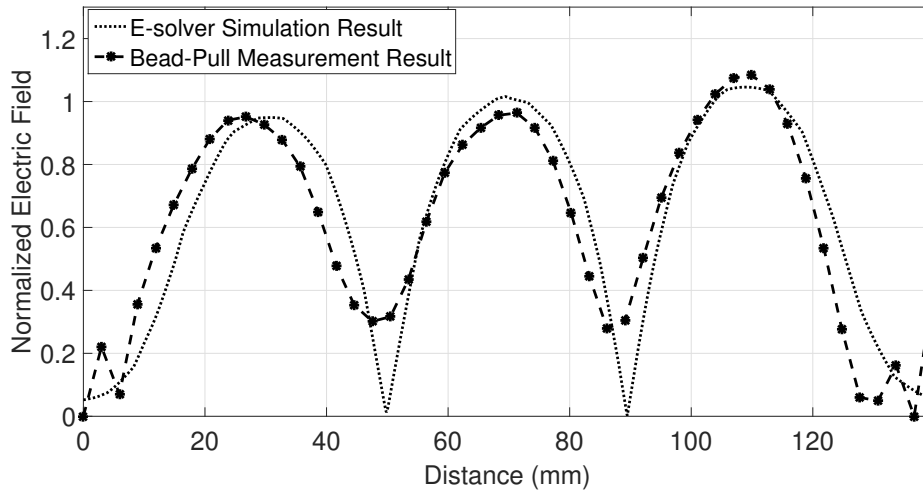
Figure 4.10. Bead-Pull Results with 4.6 mm Misalignment on Cell 1
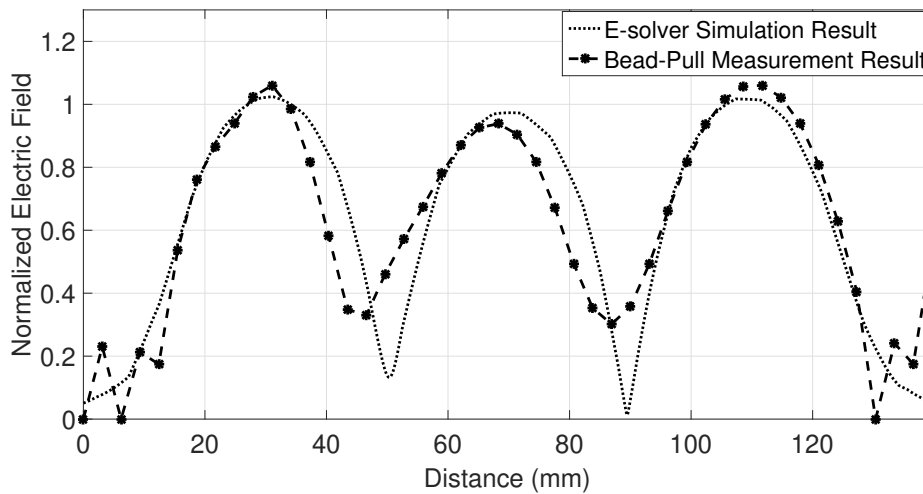
Figure 4.11. Bead-Pull Results with 4.6 mm Misalignment on Cell 2

In Figure 4.12, the experiment setup for the measurement results presented in Figure 4.9-4.11 is shown. The rope passed through the bead and the cavity is fixed to a cover clamped on the servo motor. The servo motor is driven by an Arduino and the angular position of the servo motor is adjusted via the serial port of the Arduino by using a computer. In the meantime, the VNA, which is connected to the cavity, measures the frequency value and a simple LabView code records the data on the computer.

Since the rope used in the measurement is sufficiently taut, the gravitational force

has become a negligible factor. Therefore, the difference between whether the system is horizontal or vertical becomes insignificant. Apart from the elimination of gravitational force, accurate centering of the bead is also an important consideration in the bead-pull measurement. That's why, 4 different measurements were taken as the solution to the bead centering problem and the mean values of these measurements were plotted.

Figure 4.12. Photo of Bead-Pull Measurement Setup

| (a) | (b) |

Figure 4.13. CST View of 3-cell 3.9 GHz Cavity (a) Full View (b) Cross-section

The CST model of the 3-cell 3.9 GHz cavity is given in Figure 4.13. Since the problem is evaluated in the E-solver, an excitation source is not required to obtain the

electromagnetic pattern. Note that, the blue line seen in Figure 4.13-b represents the measurement line that corresponds to the magnitude of the electric field.
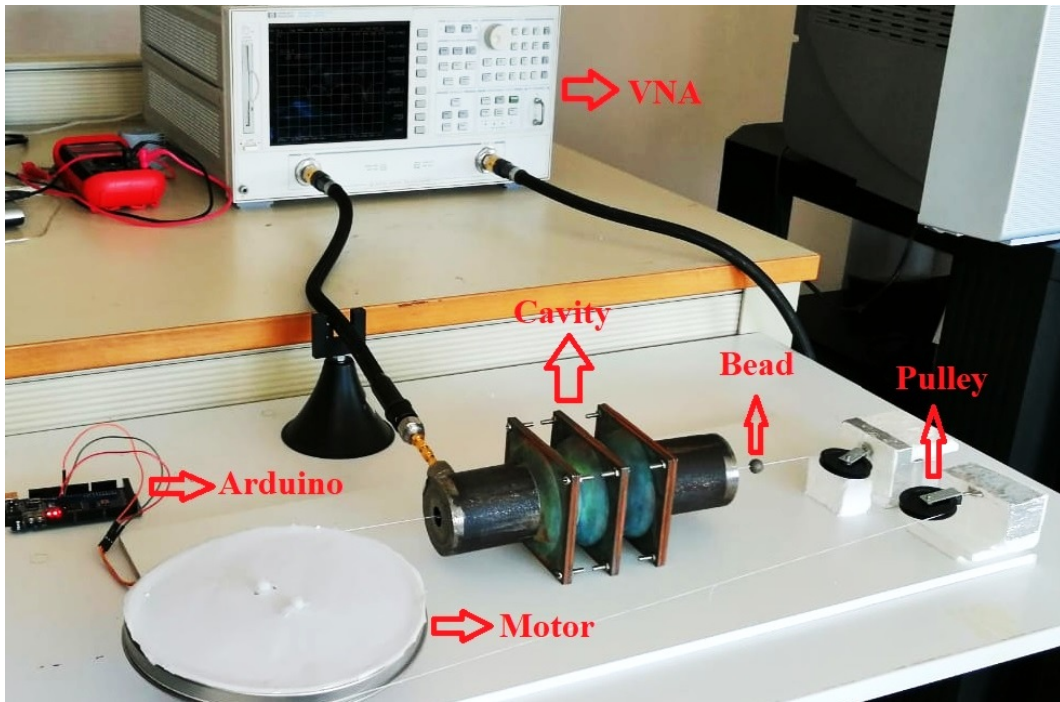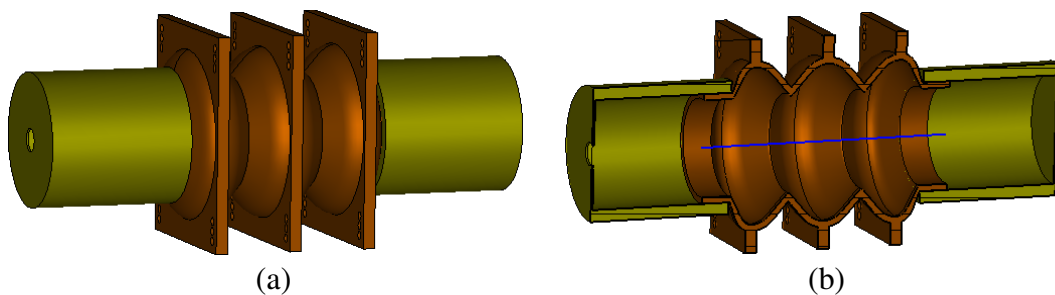
It should be noted that the field distribution inside the cavity is perturbed during the bead-pull measurement. According to a simulation result run by CST-MWS program, the electric field distribution during the bead-pull measurement is disrupted as shown in Figure 4.14. The electric field value around the bead reaches peak values, even exceeding the peaks around the iris region, which normally has the highest electric field values of the cavity. Note that the resonance region is simulated without the inclusion of the covers.
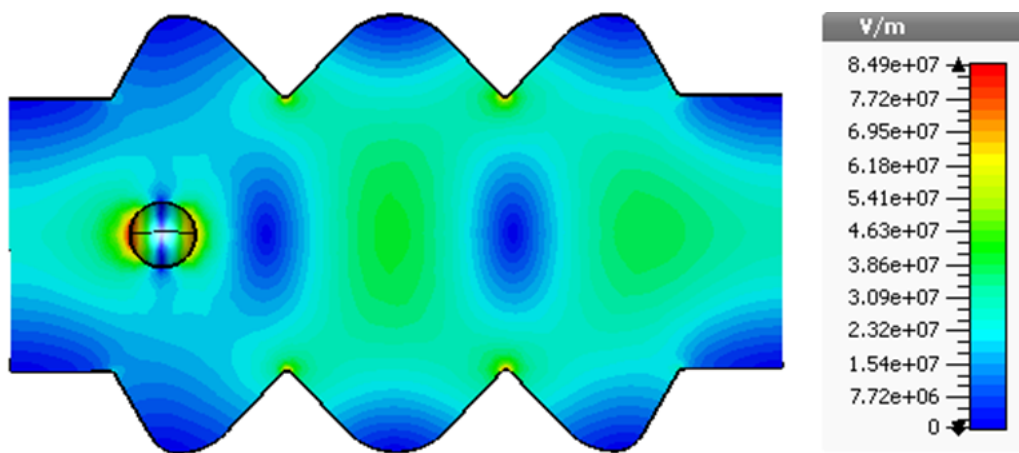
Figure 4.14. Electric Field of 3-Cell 3.9 GHz Cavity with a Metallic Bead

4.2. 1-Cell 2.45 GHz Elliptical Cavity

We repeat the experiments with a more conductive cavity for the verification of our findings. For this purpose, a single cell cavity whose π-mode resonates at 2.45 GHz was designed and fabricated. This frequency was chosen since it is in the ISM band and allows it to be fed with the commercial magnetrons for future works. Based on the TESLA-shaped cavity, an optimized cavity design at 2.45 GHz was realized. The shape of the cavity was produced by drilling only the inner volume, while the outer part remains as a bulk since field flatness tuning is not required in a single cell cavity and it is less costly to fabricate in this way. However, the fabrication of a single-cell aluminum cavity at 2.45 GHz is about 5 times more expensive than the 3-cell 3.9 GHz elliptical cavity manufactured by the 3D printer.
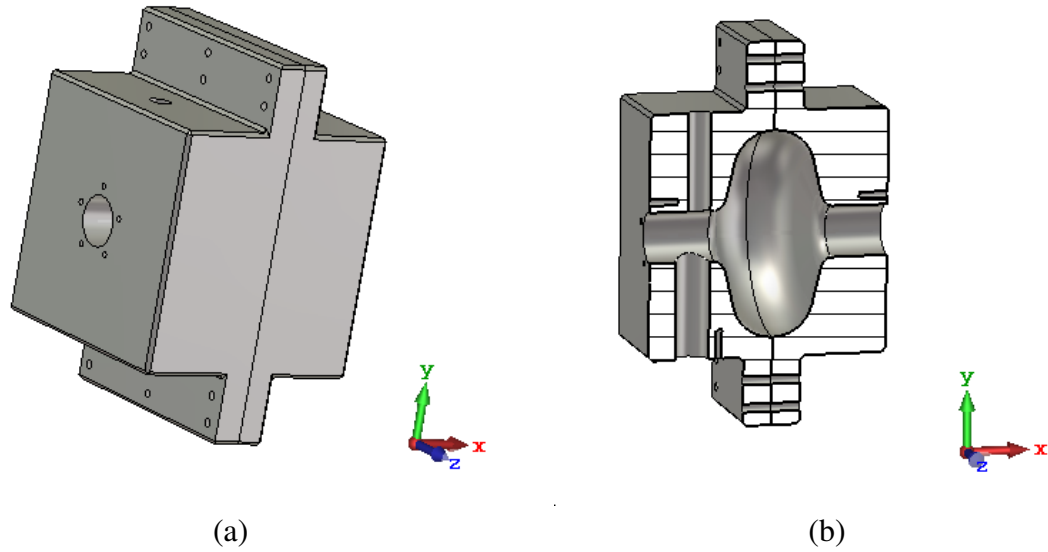
Figure 4.15. 1-Cell 2.45 GHz Elliptical Cavity (a) Full view (b) Cross-section

As can be seen in Figure 4.15, the cavity has 4 holes, 2 beam pipes and 2 power transmission points. The radii of the two holes for power transmission are different, one 10 mm and the other 6 mm. The smaller hole is designed to fit precisely to the N-type coupler, while the larger hole can be used for higher power transmissions. In addition, 5 screw holes are added to around each holes in order to keep the other holes closed while taking measurements from one hole. The fastening of 2 half-cells will also be realized by a total of 12 screw holes, that also allow the possibility of intentional misalignment, under and above the cavity. The diameter of the screw holes below and above the cavity is 4.4 mm, while the diameter of the screw holes drilled for the covers is 3.2 mm. Besides, the iris and equator diameters of the structure are 26.5 mm and 106.8 mm, respectively.

4.2.1. Fabrication of the 1-Cell 2.45 GHz Aluminum Cavity

The internal volume of the cavity can be created by engraving a block of aluminum with a CNC machine. Alternatively, a turning machine can be used, but CNC machines are more reliable in terms of surface roughness. On the other hand, although the tolerance value that can be written to the machine is 1 micrometer, the actual value is much higher. Therefore, the surface treatment must be applied after the engraving process. Screw holes and coupler holes are also drilled by using external drilling tools.

Since the cavity consists of 2 separate half-cells, it is important that the screw

holes to connect them do not cause leakage. Thus, the joint holes have been drilled, and the radii are equal to the free plug radii of M4 screws. Similar to the structure fabricated from the 3D printer, this cavity has nuts on the other side of the screws where the half-cells are attached, and the etching is provided by these nuts. The unassembled view of the 2 half-cells can be seen in Figure 4.16. When assembling these parts, at least 3 screw washers should be used for each hole, 1 for the head of the screws and 2 for the nuts.

Figure 4.16. Image of 2 Separate Half-Cells of a 1-Cell Elliptical Cavity

4.2.2. Experimental Results

As in the previous structure, frequency, quality factor and bead-pull measurements were performed for the aluminum single cell cavity. In this structure where we can obtain 1-level misalignment due to fabrication restrictions, the effect of misalignment was also observed. The transversal distance between the centers of the holes is 14.4 mm in order to create misalignment due to some mechanical limitations caused by the aluminum drilling tool. Apparently, this value is exaggerated, but it allows us to show the proof of concept.

4.2.2.1. Frequency and Quality Factor Measurements

The cavity was excited at 2.45 GHz thanks to an N-type coupler fixed to the 6 mm radius hole of the cavity and an antenna attached to end of the coupler. With the critically coupled N-type coupler, the approximate resonant frequency and half of the quality factor of the cavity can be measured. The reason for the approximate resonant frequency statement is that the antenna perturbing the cavity shifts the resonant frequency of the cavity slightly. The resonant frequency may increase or decrease, depending on whether the antenna perturbs the magnetic field or the electric field region, respectively. In addition, as mentioned earlier, multiplying the measured quality factor by 2 (more precisely, multiplying by 1+CF) provides the unloaded quality factor of the cavity.

The cavity was excited by critical coupling from the electric field region by means of a 1 mm diameter L-shaped antenna inserted through the hole having 6 mm radius in the structure. The reflection coefficient in the case of critical coupling should be obtained as close to zero as possible in linear scale, which can be checked via the Smith Chart. The measurement data recorded at 801 measuring points, and an almost perfect circle appeared, as shown in Figure 4.17-b. The impedance at the resonance frequency was very close to 50 Ω, which is 48.463 + j*0.3984 Ω. As can be seen in Figure 4.17-a, the half-cells were properly connected to each other and the open holes were closed by means of covers.

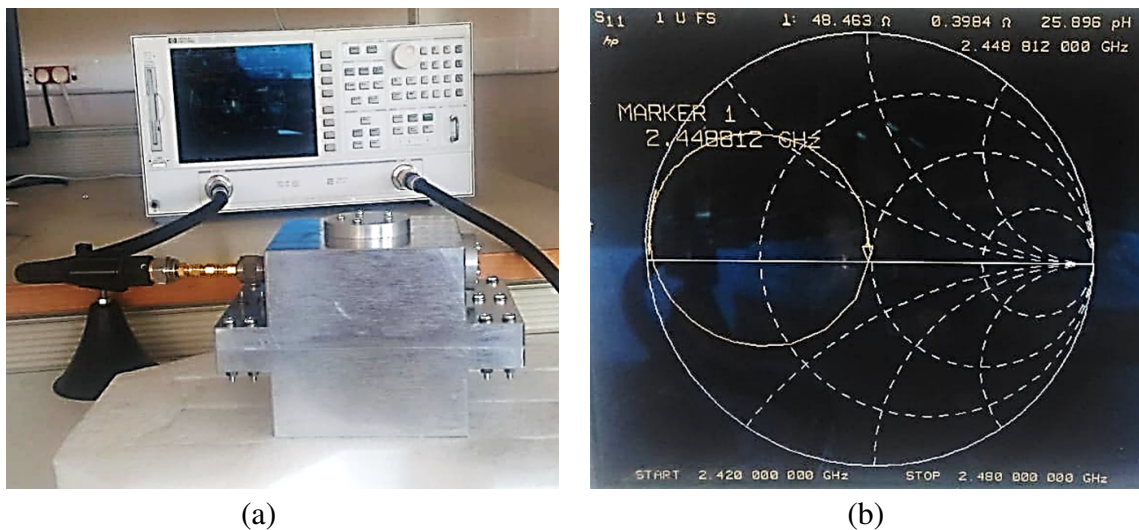(a)   (b)

Figure 4.17. Measurement of the 1-Cell 2.45 GHz Cavity (a) Experimental Setup (b) Smith Chart

In Figure 4.18, the quality factor was found in the range of 7200-7500 according to the measurement results when the cavity was precisely assembled with screws without alignment error. This value is obtained ~ 16000 in the simulation for the single cell aluminum cavity. However, the actual conductivity of aluminum may be lower than the considered value in the simulation. If the conductivity of the material in the simulation is updated to 8×10^6 S/m, approximately the same quality factor can be achieved. In addition, errors which occur during fabrication and assembly are the factors that can reduce the quality factor. Note that, although the measuring range has been narrowed down to 20 MHz, the reflection coefficient depths still seem quite narrow. The resonant frequency was slightly below 2.45 GHz in both measurement and simulation results. The main reason for this is the existence of the antenna perturbing the cavity from the electric field region. According to shape perturbation equation, the reduction of the cavity volume from the electric field region means that the resonant frequency decreases. The different resonant frequencies of the simulation and measurement can be attributed to the faults during fabrication and the different amount of insertion of the antenna into the cavity.
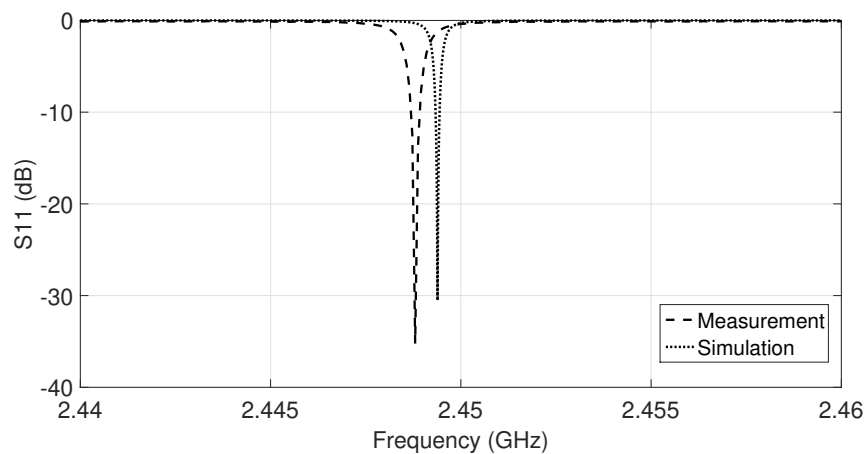
Figure 4.18. S_{11} Results of Aligned 2.45 GHz 1-Cell Elliptical Cavity

If the screws and nuts used when joining the half-cells of the cavity were not properly tightened, gaps would remain between the half-cells. The quality factor of the cavity would then be decreased dramatically. For instance, when half-cells of the cavity were to be assembled by hand instead of screws, the quality factor of the same mode was measured as 1500 instead of 7500. It has been observed that the quality factor rises as the screws and nuts tighten and converges after a certain point.

Suppose an alignment error of 14.4 mm occurs while attaching 2 half-cells. Some mechanical limitations are the reason why the alignment error is large. As a result of this misalignment, the resonant frequency shifted down by ~ 30 MHz. According to the results in Figure 4.19, the quality factor was found to be between 5200-5400 in the measurement, and this value was found ~ 12500 in the simulations. Note that, the reduction rate in quality factor is approximately the same in the measurement and simulation. If we take all of the conductivity difference and fabrication errors into the effective conductivity value, we can conclude that the geometry factor values are consistent for simulation and measurement results.
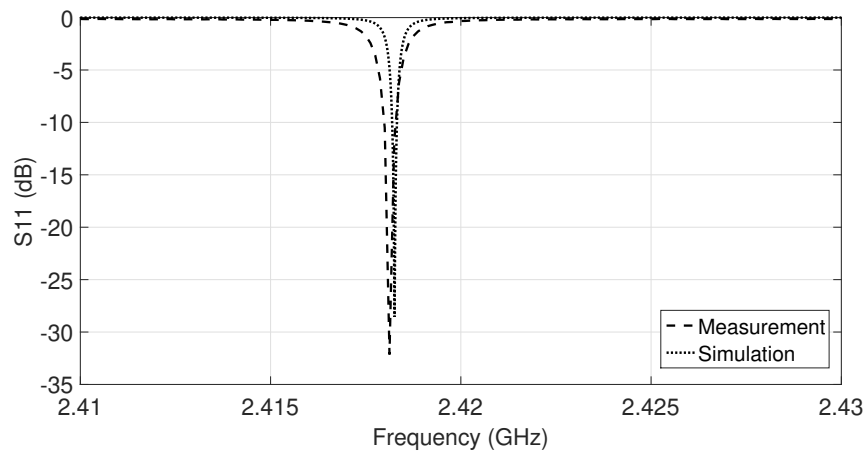
Figure 4.19. S_{11} Results of Misaligned 2.45 GHz 1-Cell Elliptical Cavity

4.2.2.2. Bead-Pull Measurement

The bead-pull setup for measuring the electric field profile of the 3-cell cavity was also used for this cavity. The 3-cell cavity in Figure 4.12 was replaced with the single cell cavity and slight changes were applied to the Arduino code as the total size of the structure changed.

According to the measurement and simulation results, the antenna must cut the beam axis in the beam-pipe region in order to excite the cavity, critically. However, this means that the bead intersects with the antenna during the bead-pull measurement. On the other hand, it is not necessary to excite the cavity critically to obtain the electric field profile. It is sufficient to excite the cavity so that the resonant frequency can be observed,

and this value is preferably below -3 dB for this experiment. The most important limitations here are the sensitivity and number of points of the VNA used. If VNA sensitivity is sufficient to observe the value of resonant frequency for all bead locations, no better coupling is required for bead-pull measurement.

Since the electric field profile in the single cell cavity does not deteriorate significantly, the main purpose of the bead-pull measurement with this cavity is to determine the geometric shunt impedance value. Since the Q and frequency values are also known, the parallel RLC equivalent circuit of the cavity can be formed (Hansen and Post, 1948). For this process, it is necessary to combine geometric shunt impedance definition with shape perturbation theory and as a result, Equation 4.3 is obtained for a spherical metallic bead (Mcintosh, 1994). If the bead had a different shape than a sphere, different coefficient would be used as a multiplier. The reader can find more detailed information in the literature (Dekleva and Robinson, 1959; Mallory and Hansen, 1958). Note that, unlike previous simulations and measurements, the integration line centers both the input and output for both aligned and misaligned case.

$$\frac{R}{Q} = \frac{\left(\int_0^L \sqrt{\frac{\Delta\omega(l)}{\omega_{mnp}}}\mathrm{d}l\right)^2}{\pi r_{bead}^3 \omega_{mnp}\epsilon_0} \tag{4.3}$$

where ω_{mnp} stands for the angular frequency of the mnpth mode of the unpertubed cavity, r_{bead} denotes the radius of the spherical bead and $\Delta\omega$ means the angular frequency shift due to perturbation. Note that the amount of frequency shift is a function of the position.

Figure 4.20 shows the bead-pull measurement results of the aligned and misaligned cases of the half-cells. If the corresponding numerical integrals are substituted into equation 4.3, the geometric shunt impedance values without considering transit time factor are found as 356.6836 and 315.6081 Ω for aligned and misaligned cases, respectively. In the simulation, these values are found to be 353.984 and 311.509 Ω. When the RLC equivalent of the cavity is to be obtained with the help of bead-pull measurement on the beam-axis, a result as in Table 4.3 is obtained. Since the geometric parameters in the measurements are almost the same as in the simulation, L and C values are very close to each other in the simulation and measurements, but the R values are different because the conductivity predicted in the simulation is different from the actual value. As predicted by the simulations of the 9-cell cavity, inductive and resistive values tend to decrease while capacitive value in parallel equivalent circuit increases with misalignment. Note that the R value in the equivalent circuit is equal to the half of the shunt impedance of the cavity.

The L and C values of the parallel equivalent circuit are calculated as given in Equations 2.34 and 2.44.
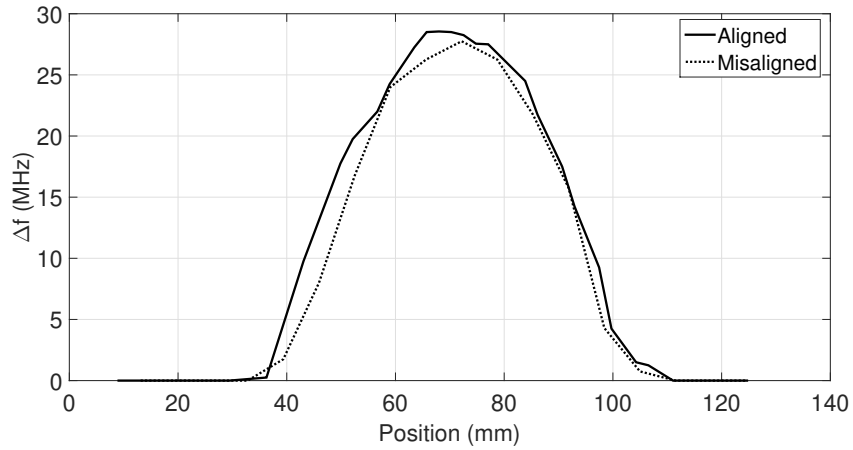
Figure 4.20. Bead-Pull Measurement Results of 1-Cell 2.45 GHz Elliptical Cavity

Table 4.3. Equivalent Parallel RLC Circuit Approach

Parameters	Measurement (Aligned)	Measurement (Misaligned)	Simulation (Aligned)	Simulation (Misaligned)
f (GHz)	2.4488	2.4181	2.4494	2.4183
Q	7500	5400	16000	12500
R_{sh}/Q (Ω)	356.684	315.608	353.984	311.509
R_{par} ($M\Omega$)	1.34	0.85	2.83	1.95
C_{par} (pF)	0.364	0.417	0.367	0.423
L_{par} (nH)	11.59	10.39	11.50	10.25

CHAPTER 5

CONCLUSION

In this study, five different elliptical cavities have been designed and two of them have been fabricated and measured. By using these cavities, it is aimed to examine the effects of some possible fabrication defects on the electromagnetic fields and particle-cavity interactions, hence to build know-how to take action if necessary. In this context, the order of importance of fabrication errors such as half-cell misalignment, surface roughness and the tuning methods are examined in details. In addition, this study has significant results in order to determine the tolerances needed for specific structures.

Thesis studies are started for a 9-cell 3.9 GHz elliptical cavity structure. Later on, the investigations are extended for the other types of cavities. The most important aspect of this cavity is that it has multicell and low CTCC, so the consequences of even small defects on the electromagnetic field can be easily observed. For this purpose, it is important to determine the dimensions of the iris radius correctly and to perform the necessary 3D electromagnetic analysis. The simulations of this cavity yield interesting results. For instance, the extent of deterioration of the parameters varies depending on the cell in which the alignment error is located. While normalized PSEF, PSMFD and geometric shunt impedance are more affected by misalignment on the end cell, the most serious decline in the geometry factor is caused by the defect on the mid cell. Furthermore, disturbances of transverse electric field and wake impedance due to misalignment are observed. For both parameters, the negative effects, e.g. transverse kick, increase when the number of misaligned cells increases. The aim of simulating 3-cell 3.9 GHz and 3-cell 2 GHz cavities and iris misalignment of 9-cell 3.9 GHz cavity is to validate the equator misalignment simulations with 9-cell 3.9 GHz cavities. It can be said that geometric shunt impedance and accordingly normalized PSEF and PSMFD values are more dependent on end cell and geometry factor is more dependent on mid cell according to the simulations performed by changing frequency and cell number. In addition, frequency shift seems to be more correlated with the middle cell, but it is difficult to mention a certainty since the amount of shift is small.

One of the major drawbacks of misalignment is the disturbance of field homogeneity, as the amplitude of the electric and magnetic field in the misaligned cell tends to decrease. We report that, it is possible to restore the peak electric field of the relevant

cell to its former value by using the conventional tuning method. When this happens, geometric shunt impedance, normalized PSEF and PSMFD parameters and percentage of field flatness return to their original values, while geometry factor and transverse kick parameters worsen. It should be noted that lower CTCC provides higher acceleration efficiency but this causes to increase geometric sensitivity which is an undesired parameter. To overcome this trade-off, it has been shown that lower geometric sensitivity may not be required for correctable parameters like normalized PSEF, PSMFD and geometric shunt impedance. Also, it should be noted that multiple alignment errors can also be exploited at least on a simulation basis and bring field flatness closer to one if it is assumed that a tuning attempt is being made by ignoring the transverse kick and geometry factor.

In the thesis studies, not only cell alignment error but also surface roughness have been simulated and the applicability of the proposed approach obtained on wake fields has been tested. The actual defects in a rectangular cavity are modeled as an empirical surface impedance, and it can be seen that the model used can also be applied to resonator structures to match the parameters in terms of metal loss and electric field amplitude. Thanks to this approach, simulation results can be reduced from more than 12 hours to 18 minutes for convergent simulation results on the same computer. Wake field simulations based on this approach show that increased surface impedance leads to a decrease in wake fields, which is an undesirable effect. In other words, an undesirable parameter can reduce another unwanted parameter. Surely, increased surface impedance can lead to breakdowns in superconducting structures, but also to high wall temperatures in normal conductive structures. However, if these problems are solved in some way, this investigation can be exploited in the future.

In the experimental part of the thesis, a resonator cavity is fabricated with a 3D printer and it is tried to increase effective conductivity with different coating methods. Electroless nickel plating and copper electroplating processes show that the effective conductivity has increased to 5 times by plating copper on the nickel via electrolysis. By means of this inexpensive method, the effect of equator alignment error on the material independent parameters such as geometry factor, frequency shift and field flatness can be experimentally investigated and which cell is more effective on these parameters can be determined. Demonstrating the applicability of such a cost-effective method for defect analysis is one of the important contributions of this thesis. In addition, a single cell 2.45 GHz aluminum elliptical cavity is fabricated and the quality factor is measured ~ 7500 via of critical coupling measurement technique. In addition to the critical coupling measurements with reflection coefficients below -30 dB with appropriate antenna

sizes, bead-pull measurements are also performed and the parallel RLC equivalent of the circuit is obtained in the light of the data obtained from these measurements. With these measurements, it is observed that the misalignment increases the capacitive value of the cavity and decreases the inductive and resistive values.

Overall, this thesis tries to shed light on new productions by focusing on the problems and possible solutions caused by mechanical errors in the fabrication of elliptical accelerator cavities which are very expensive devices to realize precisely. Simulation-based and experimental investigations have yielded interesting and important results and information that can be used in future fabrications has been revealed.

REFERENCES

Akcelik, V., L.-Q. Lee, Z. Li, C.-K. Ng, L. Xiao, and K. Ko (2008). Srf cavity imperfection studies using advanced shape uncertainty quantification tools. In *Proceedings of Linac08*, pp. 870–872.

Bahng, J., E.-S. Kim, B.-H. Choi, and B.-H. Choi (2017). Development of rfq for bnct accelerator. In *Proceedings of IPAC2017*, Copenhagen, Denmark, pp. 4260–4262.

Bal, A., D. Carey, F. Espinal, and G. Huff (2019). Electroless silver plating of 3d printed waveguide components by peristaltic pump driven system. *Electron. Lett. 55*(2), 100–102.

Balanis, C. (1989). *Advanced engineering electromagnetics*. New York: Wiley.

Banford, A. P. and G. H. Stafford (1961). The feasibility of a superconducting proton linear accelerator. *Plasma Physics (J. Nucl. Energy Part C) 3*, 287–290.

Barbanotti, S., I. Gonin, C. Grimm, T. Khabibouline, M. Foley, L. Ristori, N. Solyak, and V. Yakovlev (2010). Status of the design of 650 mhz elliptical cavities for project x. In *Proceeding of Linear Accelerator Conference LINAC2010*, Tsukuba, Japan, pp. 289–291.

Bellantoni, L., H. Edwards, T. Khabibouline, and A. Rowe (2003). Field flatness tuning of tm110 mode cavities with closely spaced modes. In *Proceedings of the 11th Workshop on RF Superconductivity*, Luebeck/Travemuender, Germany, pp. 265–268.

Brown, P., O. Brunner, A. Butterworth, E. Ciapala, H. Frischholz, G. Geschonke, E. Peschardt, and J. P. H. Sladen (2001). Operating experience with the lep2 superconducting rf system. In *The 10th Workshop on RF Superconductivity*, pp. 185–193.

Caspers, F. (2012). Rf engineering basic concepts: the smith chart. Technical Report arXiv:1201.4068, CERN, Geneva, Switzerland.

Chao, A. W. and M. Tigner (1999). *Handbook of Accelerator Physics and Engineering*.

Singapore: World Scientific.

Chodorow, M., E. L. Ginzton, I. R. Neilson, and S. Sonkin (1953). Design and performance of a high-power pulsed klystron. *Proc. IRE 41*(11), 1584–1602.

Crookes, W. (1878). On the illumination of lines of molecular pressure, and the trajectory of molecules. *Phil. Trans. 28*(170), 135–164.

Cuttone, G. (2008). Applications of particle accelerators in medical physics. Technical Report CERN-KTT-2013-001, CERN.

Dekleva, J. and K. Robinson (1959). Simple method of shunt impedance measurement. *The Review of Scientific Instruments 30*(6), 470–471.

Delayen, J. (2008, 6). Cavity fabrication. In *USPAS 2008*, U. Maryland, USA.

Delayen, J. R. (2010). Applications of spoke cavities*. In *Proceedings of Linear Accelerator Conference LINAC2010*, pp. 377–381.

Ebeling, F., R. Klatt, F. Krawczyk, E. Lawinsky, T. Weiland, S. G. Wipf, B. Steffen, T. Barts, M. J. Browman, R. K. Cooper, H. Deaven, and G. Rodenz (1989, July). The 3-d mafia group of electromagnetic codes. *IEEE Transactions on Magnetics 25*(4), 2962–2964.

Fawole, O. and M. Tabib-Azar (2016). Multimode rectangular cavity terahertz resonators. In *2016 IEEE MTT-S International Wireless Symposium (IWS)*, Shanghai, China, pp. 1–4.

Fujita, K., H. Kawaguchi, T. Weiland, and S. Tomioka (2009). Three-dimensional wake field computations based on scattered-field time domain boundary element method. *IEEE Trans. Nucl. Sci. 56*(4), 2341–2350.

Fujita, K., H. Kawaguchi, I. Zagorodnov, and T. Weiland (2006). Time domain wake field computation with boundary element method. *IEEE Trans. Nucl. Sci. 53*(2), 431–439.

Gold, G. and K. Helmreich (2015). Surface impedance concept for modeling conductor

roughness. In *2015 IEEE MTT-S International Microwave Symposium*, pp. 1–4.

Halbach, K. and R. Holsinger (1976). Superfish-a computer program for evaluation of rf cavities with cylindrical symmetry. *Particle Accelerators 7*, 213–222.

Hall, S., S. Pytel, P. Huray, D.Hua, A. Moonshiram, G. Brist, and E. Sijercic (2007). Multigigahertz causal transmission line modelling methodology using a 3-d hemispherical surface roughness approach. *IEEE Trans. Micro. Theo. Tech. 55*(12), 2614–2624.

Hammerstad, E. and O. Jensen (1980). Accurate models for microstrip computer-aided design. In *1980 IEEE MTT-S International Microwave symposium Digest*, pp. 407–409.

Hansborough, L. D., J. M. Potter, and N. G. Wilson (1981). Mechanical design of rfq resonator cavities in the 400-mhz frequency range. In *Proceedings of the 1981 Linear Accelerator Conference*, pp. 329–331.

Hansen, W. (1938). A type of electrical resonator. *J. Appl. Phys. 9*(10), 654–663.

Hansen, W. and R. Post (1948). On the measurement of cavity impedance. *Journal of Applied Physics 19*, 1059–1061.

Harrington, R. F. (1961). *Time-Harmonic Electromagnetic Fields*. New York: McGraw-Hill.

Hill, D. (2009). *Electromagnetic Fields in Cavities: Deterministic and Statistical Theories*. Piscataway, N.J: IEEE.

Huray, P., S. Hall, S. Pytel, F. Oluwafemi, R. Mellitz, D. Hua, and P. Ye (2007). Fundamentals of a 3-d snowball model for surface roughness power losses. In *2007 IEEE Workshop on Signal Propagation on Interconnects*, pp. 121–124.

Huray, P., F. Oluwafemi, J. Loyer, E. Bogatin, and X. Ye (2010). Impact of copper surface texture on loss: A model that works. In *DesignCon 2010 Proceedings*, pp. 1–22.

Ising, G. (1924). Prinzip einer Methode zur Herstellung von Kanalstrahlen hoher Voltzahl. *Ark. Mat. Astron. Fys. 18*(30), 1–4.

Juntong, N. (2011). *Investigation of Optimised Electromagnetic Fields in SRF Cavities for the ILC*. Ph. D. thesis, The University of Manchester, England.

Karatay, A. and F. Yaman (2018, 9). Electromagnetic simulations of mechanical imperfections for elliptical cavities. In *Turkish Physical Society 34th International Physics Congress*, Bodrum, Turkey.

Karatay, A. and F. Yaman (2019a). Electromagnetic Simulations of Mechanical Imperfections for Accelerator Cavities. *IEEE Trans. Nucl. Sci. 66*(11), 2295 – 2304.

Karatay, A. and F. Yaman (2019b). Fully 3d printed bead-pull measurement of an elliptical cavity. In *Book of Full Text Proceedings Turkish Physical Society 35th International Physics Congress (TPS35)*, Volume 01, Bodrum, Turkey, pp. 42–49.

Kilpatrick, W. (1957). Criterion for vacuum sparking designed to include both rf and dc. *Rev. Sci. Instrum. 28*(10), 824–826.

Kyovtorov, V., I. Georgiev, S. Margenov, D. Stoychev, F. Oliveri, and D. Tarchi (2017). New antenna design approach - 3d polymer printing and metallization, experimental test at 14-18 ghz. *Int. J. Electron. Commun. (AEUE) 73*, 119–128.

Li, Z. and C. Adolphsen (2008). A new srf cavity shape with minimized surface electric and magnetic fields for the ilc. In *IProceedings of LINAC08, Victoria, BC, Canada*, pp. 867–869.

Liebig, T. A. R., S. Held, and D. Erni (2013). Openems - a free and open source equivalent-circuit (ec) fdtd simulation platform supporting cylindrical coordinates suitable for the analysis of traveling wave mri applications. *Int. J. Numer. Model. 26*, 680–696.

Lomakin, K., G. Gold, and K. Helmreich (2017). Transmission line model for rectangular waveguides accurately incorporating loss effects. In *2017 IEEE 21st Workshop on Signal and Power Integrity (SPI)*, pp. 917–920.

Lomakin, K., G. Gold, and K. Helmreich (2018). Analytical waveguide model precisely predicting loss and delay including surface roughness. *IEEE Trans. Micro. Theo. Tech. 66*(6), 2649 – 2662.

Mallory, K. and W. Hansen (1958). Measurement of shunt impedance of a cavity. *Journal of Applied Physics 29*(5), 790–793.

Marhauser, F. (2011). Jlab srf cavity fabrication errors, consequences and lessons learned. In *Proceedings of IPAC2015*, pp. 346–348.

Mcintosh, P. (1994). Perturbation measurements on rf cavities at daresbury. In *4th European Particle Accelerator Conference*, London, UK, pp. 1283–1285.

MG-Chemicals (2013). Super shield tm conductive nickel coating 841 technical data sheet. https://www.alliedelec.com/m/d/5f9e9d126658bbb4e314280cf3f93cb0.pdf.

Mittal, K. C., J. Mondal, S. Ghatak, A. S. Dhavale, S. R. Ghodke, R. S. Vohra, S. B. Jawale, D. Dutta, P. K. Pujari, T. K. Saha, and A. V. Bapat (2011). Ingot niobium rf cavity design and development at barc. In *Symposium on the Superconducting Science and Technology of Ingot Niobium*, pp. 100–115.

Nassiri, A., B. Chase, P. Craievich, A. Fabris, H. Frischholz, J. Jacob, E. Jensen, M. Jensen, R. Kustom, and R. Pasquinelli (2016). History and technology developments of radio frequency (rf) systems for particle accelerators. *IEEE Trans. Nucl. Sci. 63*(2), 707–750.

Nelatury, S. and C. Nelatury (2014). A comparison of perturbation formulas for a square electromagnetic resonator. *IEEE Antennas and Propagation Magazine 56*(1), 132–142.

Novokhatski, A. (2012). A new green's function for the wake potential calculation of the slac s-band constant gradient accelerating section. *Nucl. Instrum. Methods Phys. Res. - A 684*, 46–51.

Novokhatski, A. and A. Mosnier (2014). Short bunch wake potentials for a chain of tesla cavities. *Nucl. Instrum. Methods Phys. Res - A 763*, 202–209.

Olry, G. and B. Leluan (2001). Precise 3d geometrical control of 700 mhz sc elliptical cavities: Rf measurements vs theoretical simulations. In *The 10th Workshop on RF Superconductivity*, pp. 437–440.

Ozcan, M. (2018). Rf doğrusal hızlandırıcı kovuk ve fotokatot rf-tabanca tasarımı ve simülasyon çalışmaları. Master's thesis, Hacettepe Üniversitesi, Turkey.

Padamsee, H. (2017). 50 years of success for srf accelerators-a review. *Supercond. Sci. Technol. 30*, 1–23.

Pagani, C., D. Barni, A. Bosotti, and P. Pierini (2001). Design criteria for elliptical cavities. In *The 10th Workshop on RF Superconductivity*, Tsukuba, Japan, pp. 115–122.

Palumbo, L., V. Vaccaro, and M. Zobov (1994, 9). Wake fields and impedance. In *CAS Advanced School on Accelerator Physics*, Rhodes, Greece, pp. 1–70.

Porsuk, D. (2015). Süper iletken ve normal iletken hızlandırıcılarda kavite dizaynı ve hızlandırıcı sistemlerin modellenmesi. Master's thesis, Dumlupınar Üniversitesi.

Pozar, D. M. (2005). *Microwave engineering; 3rd ed.* Hoboken, NJ: Wiley.

Saha, T., J. Mondal, K. C. Mittal, K. G. Bhushan, and A. V. Bapat (2012). Fabrication of niobium superconducting accelerator cavity by electron beam welded joints. In *International Symposium on Vacuum Science Technology and Its Application for Accelerators*, pp. 1–8.

Sekutowicz, J. (2012). Superconducting elliptical cavities. Technical Report arXiv:1201.2598 [physics.acc-ph], ArXiV.

Sekutowicz, J., G. Ciovati, P. Kneisel, G. Wu, A. Brinkmann, W. Hartung, R. Parodi, and S. Zheng (2003). Cavities for jlab's 12 gev upgrade. In *Proceedings of the 2003 Particle Accelerator Conference*, pp. 1395–1397.

Simonovich, L. (2016). Practical method for modeling conductor surface roughness using cubic close-packing of equal spheres. In *2016 IEEE International Symposium on Electromagnetic Compatibility*, pp. 917–920.

Singer, W. (2017). Fabrication of elliptical srf cavities. *Supercond. Sci. Technol. 30*(033001), 1–14.

Spielman, B. (2006). Effects of wall perturbations on tm modes in arbitrarily-shaped cylindrical wave guides. In *2006 IEEE MTT-S International Microwave Symposium Digest*, San Francisco, CA, USA, pp. 1009–1012.

Stern, H. A., D. R. Sadoway, and J. W. Tester (2011). Copper sulfate reference electrode. *J. Electroanal. Chem. 659*, 143–150.

Sulimov, A. (2015). Rf analysis of equator welding stability for the european xfel cavities. In *Proceedings of SRF2015*, pp. 1272–1273.

Sulimov, A., A. Gresele, M. Giaretta, and A. Visentin (2016). Rf analysis of electropolishing for exfel cavities production at ettore zanon spa. In *28th Linear Accelerator Conference*, Geneva, Switzerland, pp. 1–3.

Sulimov, A., G. Kreps, and J. Sekutowicz (2013). Estimation of small geometry deviation for tesla-shape cavities due to inner surface polishing. In *Proceedings of SRF2013*, pp. 537–539.

Tak, J., D. Kang, and J. Choi (2017). A lightweight waveguide horn antenna made via 3d printing and conductive spray coating. *Microw Opt Tech Lett 59*(3), 727–729.

Tsakanian, A., M. Dohlus, and I. Zagorodnov (2011). Short range wake potentials of flash resistive tapered collimator and european xfel undulator intersection. *Nucl. Instrum. Methods Phys. Res - A 659*, 9–13.

Van de Graaff, R. J., K. T. Compton, and L. C. Van Atta (1933). The electrostatic production of high voltage for nuclear investigations. *Phys. Rev. 43*, 149–157.

Varian, R. and S. Varian (1939). A high frequency oscillator and amplifier. *J. Appl. Phys. 10*(5), 321–327.

Vostrikov, A. (2015, 8). *Physics and Material Science of Ultra-High Quality Factor Superconducting Resonator*. Ph. D. thesis, The University of Chicago, Chicago, Illinois.

Wang, H., R. Rimmer, and G. Wu (2005). Elliptical cavity shape optimization for acceleration and hom damping. In *Proceedings of 2005 Particle Accelerator Conference*, Knoxville, Tennessee, pp. 4191–4193.

Wang, J. W., S. G. Tantawi, C. Xu, M. Franzi, P. Krejcik, G. Bowden, S. Condamoor, Y. Ding, V. Dolgashev, J. Eichner, A. Haase, J. R. Lewandowski, and L. Xiao (2017, Nov). Development for a supercompact x-band pulse compression system and its application at slac. *Phys. Rev. Accel. Beams 20*, 110401.

Wangler, T. P. (1998). *RF linear accelerators*. United States of America: Wiley.

Wideroe, R. (1928). Über ein neues Prinzip zur Herstellung hoher Spannungen. *Arch. Elektrotech 4*(21), 387–406.

Wilson, P. B., H. A. Schwettman, and W. M. Fairbank (1963). Status of research at stanford university on superconducting electron linacs. In *Proc. 4th Int. Conf. on High Energy Accelerators*, pp. 694–699.

Xiao, B., S. Belomestnykh, I. Ben-Zvi, J. C. Brutus, A. Fedotov, G. McIntyre, K. lo, V. Veshcherevich, Q. Wu, W. Xu, and A. Zaltsman (2015). Design of normal conducting 704 mhz and 2.1 ghz cavities for lerec linac. In *6th Particle Accelerator Conference (IPAC'15)*, pp. 3634–3637.

Xiao, L., C. Adolphsen, V. Akcelik, A. Kabel, K. Ko, L. Lee, Z. Li, and C. Ng (2007). Modeling imperfection effects on dipole modes in tesla cavity. In *Proceedings of PAC07*, pp. 2454–2456.

Zhao, F. C., H. Sun, J. Gu, M. Q. Ge, H. Shi, W. L. Huang, and S. C. Zhao (2007). Development of single cell superconducting elliptical cavity (beta=0.45) and srf test facility in ihep. In *Proceedings of SRF2007*, pp. 353–355.

Zotter, B. and S. Kheifets (1998). *Impedances and Wakes in High-Energy Particle Accelerators*. Singapore: World Sci Publishing.